Integrating suspended sediment flux in large, morphologically complex river channels: Application of a synoptic Rouse-based model to the Irrawaddy and Salween rivers

J. Jotautas Baronas[1], Emily I. Stevenson[1], Christopher R. Hackney[2,3], Stephen E. Darby[4], Michael J. Bickle[1], Robert G. Hilton[5], Christina S. Larkin[1], Daniel R. Parsons[2], Aung Myo Khaing[6], Edward T. Tipper[1]

[1]Dept. of Earth Sciences, University of Cambridge, UK
[2]Energy and Environmental Institute, University of Hull, UK
[3]School of Geography, Politics and Sociology, Newcastle University, UK
[4]School of Geography and Environmental Science, University of Southampton, UK
[5]Dept. of Geography, Durham University, UK
[6]Directorate of Water Resources and Improvement of River Systems, Yangon, Myanmar

Key Points:

- An updated empirical Rouse modeling framework to calculate sediment flux and composition in large, hydrodynamic rivers.
- Model applied to compute annual sediment flux of Irrawaddy and Salween rivers as 326^{+91}_{-70} and 159^{+78}_{-51} Mt/yr, respectively.
- Fluxes calculated using simple means of depth point samples result in errors of up to 50% relative to Rouse-based model.

Corresponding author: J. Jotautas Baronas, jotautas.baronas@gmail.com

Abstract

A large portion of freshwater and sediment is exported to the ocean by a small number of major rivers. Many of these mega-rivers are subject to substantial anthropogenic pressures, which are having a major impact on water and sediment delivery to deltaic ecosystems. Due to hydrodynamic sorting, sediment grain size and composition varies strongly with depth and across the channel in large rivers, complicating flux quantification. To account for this, we modified a semi-empirical Rouse model, synoptically predicting sediment concentration, grain size distribution, and organic carbon (%OC) composition with depth and across the river channel. Using suspended sediment depth samples and flow velocity data, we applied this model to calculate sediment fluxes of the Irrawaddy and the Salween, the last two free-flowing mega-rivers in Southeast Asia. Deriving sediment-discharge rating curves, we calculated an annual sediment flux of 326^{+91}_{-70} Mt/yr for the Irrawaddy and 159^{+78}_{-51} Mt/yr for the Salween, together exporting 46% as much sediment as the Ganges-Brahmaputra system. The mean flux-weighted sediment exported by the Irrawaddy is significantly coarser ($D_{84} = 193 \pm 13\ \mu m$) and OC-poorer ($0.29 \pm 0.08\ wt\%$) compared to the Salween ($112 \pm 27\ \mu m$ and $0.59 \pm 0.16\ wt\%$, respectively). Both rivers export similar amounts of particulate organic carbon, with a total of $1.9^{+1.4}_{-0.9}$ Mt C/yr, 53% as much as the Ganges-Brahmaputra. These results underline the global significance of the Irrawaddy and Salween rivers and warrant continued monitoring of their sediment flux, given the increasing anthropogenic pressures on these river basins.

1 Introduction

Rivers are the main conduits of dissolved and particulate matter from the continents to the oceans. Accurate quantification of material exported by rivers is thus often the most reliable and efficient way to constrain such key processes as continental erosion, chemical weathering, and organic carbon cycling (e.g., Meybeck, 1987; Gaillardet et al., 1999; West et al., 2005; Viers et al., 2013; Galy et al., 2015; Horan et al., 2019), leading to an improved understanding of the long-term controls on Earth surface conditions (e.g., Mackenzie & Garrels, 1966; France-Lanord & Derry, 1997; Berner & Kothavala, 2001; Godderis et al., 2009; Maher & Chamberlain, 2014; Hilton et al., 2015), as well as the anthropogenic perturbation of these processes (e.g., Wilkinson & McElroy, 2007; Allison et al., 2007; Syvitski & Kettner, 2011; Best, 2019). On a global scale, the world's 30 largest rivers by discharge are estimated to account for ∼50% of all freshwater and ∼25% of all particulate matter export to the ocean (Milliman & Farnsworth, 2011). Southeast Asian rivers in particular dominate the global sediment flux, delivering about 2/3 of the supply to the ocean, due to a combination of active tectonics and monsoonal climate (Milliman & Farnsworth, 2011). The sediment fluxes of the Ganges-Brahmaputra, Mekong, Irrawaddy, and other major Southeast Asian rivers maintain extensive and fertile deltas, supporting large natural and agricultural ecosystems – the primary food source for several hundred million people. In addition, the tropical monsoonal climate enables high net primary productivity and efficient export and oceanic burial of biospheric carbon – an important sink for atmospheric CO_2 (e.g., Galy et al., 2007; Hilton et al., 2008; Galy et al., 2015). Constraining the sediment and particulate organic carbon flux of large Southeast Asian rivers can help significantly reduce uncertainties in the global exogenic carbon cycle, helping both determine the importance of natural feedback processes, as well as the scale of human perturbation in these river basins.

Accurately measuring the total sediment flux and its mean physicochemical composition is difficult in large rivers due to hydrodynamic sorting of sediments, which results in strong gradients in sediment grain size, concentration and mineral composition with depth (Rouse, 1950; Dietrich, 1982; Jordan, 1965). Although turbulent shear forces affect all particles equally, heavier (larger and denser) particles have higher

settling velocities (Rouse, 1950; Dietrich, 1982). Suspended sediment concentration (SSC) at the surface is therefore not representative of the total sediment flux, which may be assessed by collecting discrete instantaneous samples at different depths, or by collecting a single depth-integrated sample, where the sampler is filled at a constant rate while being vertically lifted through the water column; however, it is often unclear how representative single depth-integrated samples are, as the quality of integration strongly depends on sampler geometry, the speed at which the sampler is lifted through the water column, and the ability to maintain isokinetic sampling conditions (e.g., Murray Hicks & Gomez, 2016). The point-sampling approach has a major advantage, in that it allows an empirical calibration of sediment concentration as a function of flow conditions specific to each sample in the river reach of interest, potentially enabling the mapping of sediment load synoptically (with depth and across the river channel).

To date, most sediment flux and composition estimates of large rivers still rely on surface samples, with the notable exceptions being the Amazon and its major tributaries (Bouchez, Lupker, et al., 2011), Ganges (Lupker et al., 2011), Changjiang (Guo & He, 2011), Mekong (Darby et al., 2016), Huanghe (Wang et al., 2007), Orinoco (Meade, 1994), and Mississippi (Meade & Stevens, 1990) rivers, which all have estimates derived via depth- and cross-channel sampling. A previously reported Irrawaddy River flux is also based on depth sampling, however, primarily using data collected in the 19th century using techniques which have since been significantly refined (Gordon, 1880; Robinson et al., 2007); see discussion below. All of the above-mentioned point-sampling studies of large rivers have revealed large variations in sediment concentration and composition with depth, indicating the need for depth (and lateral) sampling to obtain accurate estimates of sediment concentration and flux.

With the advent of Acoustic Doppler Current Profiler (ADCP) technology, it is now relatively simple and routine to measure flow velocity distribution in two dimensions (laterally and with depth) with sub-meter resolution in large river channels (e.g., Yorke & Oberg, 2002; Thorne & Hanes, 2002; Parsons et al., 2013). As a result, a number of attempts have been made to obtain a fully parametrized law for hydrodynamic sorting, which would allow the use of flow velocity data to predict sediment distribution across a river channel, with the need of just a few reference point samples. These attempts have revealed that the original Rouse model (Rouse, 1950) is unable to properly parametrize sediment distributions as function of velocity and depth, whether in large rivers (Bouchez, Métivier, et al., 2011; Lupker et al., 2011), or in flume experiments (Muste et al., 2005, and references therein). The possible reasons are the complex distribution of particle sizes and shapes (Lupker et al., 2011), particle aggregation due to organic matter (Bouchez, Métivier, et al., 2011), and the complex variation of the water and sediment diffusivity coefficients with sediment concentration (Muste et al., 2005; Pal & Ghoshal, 2016).

As an alternative, a number of indirect (surrogate) methods to determine riverine suspended loads, relying on optical and acoustic detection of sediments, have been tested (e.g., Gray & Gartner, 2009; Armijos et al., 2017). In particular, ADCP instruments determine water flow velocity by using the acoustic echo from suspended particles, potentially allowing the simultaneous quantification of SSC with depth and across the river channel with high resolution (e.g., Thorne & Hanes, 2002). ADCP backscatter signal was successfully calibrated to calculate sediment flux of the Mekong River (Darby et al., 2016) and more recently, the Paraña River (Szupiany et al., 2019). A number of complications have so far limited the applicability of this approach, however. Firstly, acoustic instruments have variable sensitivity to different particles, most strongly impacted by grain size. Therefore, a single-frequency instrument is often unable to capture SSC variations in large rivers with complex, often multi-model particle size distributions and/or variable hydrodynamic conditions (e.g., Latosinski et

al., 2014). Secondly, the calibration is typically instrument-specific such that raw data between two instruments (even of the same model) may not be comparable, requiring individual calibration for each acoustic instrument.

As a result, a hybrid empirical-theoretical approach based on the Rouse equation (Rouse, 1950, see Section 3) has emerged as a robust way to quantify suspended sediment flux and chemical composition in large rivers with complex particle size distributions and/or highly variable hydrodynamic conditions (Bouchez, Lupker, et al., 2011; Lupker et al., 2011). Instead of attempting to calibrate acoustic or optical sensing instruments, or to determine particle settling velocities for a fully theoretical prediction of SSC, point depth samples are collected to empirically calibrate the SSC-depth relationship under known hydrodynamic conditions (determined using ADCP). This approach assumes that instantaneous point samples are representative of equilibrium conditions (i.e., there is no net sediment suspension/deposition within the immediate channel reach). Any resulting error due to short-term turbulent fluctuations (e.g., Diplas et al., 2008) can be mitigated by collecting and averaging a larger number of samples (keeping in mind logistical constraints). This empirical calibration is repeated under different hydrodynamic conditions, which enables the construction of a SSC-discharge rating curve. Lupker et al. (2011) have demonstrated how point depth-sampling coupled with ADCP velocity measurements can enable more robust estimates of sediment flux, especially in kilometer-scale wide river channels with complex hydrodynamics and large lateral variations in flow velocity and sediment flux.

Here, we present an alternative approach to empirically calibrating the Rouse equation describing the SSC vs. depth vs. flow velocity relationship, and apply this framework to the Irrawaddy and the Salween rivers in Myanmar. In contrast to previous efforts, this method makes fewer averaging assumptions and allows us to synoptically map high-resolution spatial variations in sediment concentration and composition both across the river channel and with depth. We use this approach to provide new estimates of the sediment and particulate organic carbon export flux by the Irrawaddy-Salween river system and compare them to values obtained using simple averaging approach, as well as previously published estimates.

2 Methods

2.1 Study site

The Irrawaddy (also known as Ayeyarwady) and the Salween (also known as Thanlwein) are believed to be among the largest rivers in terms of water and sediment flux globally, although previous data are scarce (Robinson et al., 2007; Furuichi et al., 2009; Chapman et al., 2015). The headwaters of the Irrawaddy originate in the southern margin of the eastern Himalayan Syntaxis. It runs for about 2000 km, spanning the whole length of Myanmar and forming a large delta distributary network in the south prior to discharging into the Andaman Sea, with a basin surface area (taking topographic roughness into account using a 90m-resolution DEM) of 437,000 km^2. The Salween originates in the Tibetan Plateau, traverses the Syntaxis, and flows south across the Shan Plateau in southeastern Myanmar. It has a length of around 2800 km and a basin surface area of 283,000 km^2 (Fig. 1a). The Irrawaddy basin has a large central (relatively dry) valley, with a mean and maximum elevation of 862 and 5798 m, respectively, and a median slope of 7.1 degrees. In contrast, the Salween catchment is steep and narrow for such a large basin, with a mean and maximum elevation of 3515 and 6857 m, respectively, and a median slope of 16.4 degrees.

Both river basins are comprised of a wide variety of sedimentary, igneous and metamorphic rocks, ranging from Pre-Cambrian to Cenozoic in age and transposed by a complex network of sutures and faults (e.g., Searle et al., 2007; Mitchell et al.,

2012; Licht et al., 2013; Khin Zaw et al., 2017; Zhang et al., 2018; Westerweel et al., 2019; Najman et al., 2020). The climate of both basins is dominated by the southwest Asian monsoon (and to a lesser degree the northeast monsoon), with most precipitation and discharge taking place in June through September (Khin Zaw et al., 2017). Mean annual precipitation rates vary from <800mm/yr up to >4000 mm/yr within the Irrawaddy basin, depending on the location (e.g., Chen et al., 2017; Sein et al., 2018). Most water to both rivers is supplied by the monsoon precipitation, with additional (unquantified, but likely minor and further diminishing) inputs from mountain glacier melt and snowmelt in the north.

In terms of water and sediment flux and their chemical composition, the Irrawaddy and the Salween have very little data available compared to other Asian megarivers, largely due to historically difficult access to the country of Myanmar, which contains the major portions of both catchments (Fig. 1). The little data that are available point to the Irrawaddy-Salween system being a globally significant source of sediment and POC to the ocean but these estimates have a large uncertainty (Robinson et al., 2007; Bird et al., 2008; Furuichi et al., 2009). The Irrawaddy-Salween have remained largely undammed, with free flowing mainstems (Grill et al., 2019) and only several small dams on minor tributaries, totalling around 2500 MW generation capacity across both basins. However, over 40 dams, ranging from small to very large (>5000 MW) have been announced and are either in planning or construction stage on the two rivers, with a total capacity of more than 45000 MW (Kirchherr et al., 2017; Lazarus et al., 2019), which will significantly alter their water and sediment discharge dynamics. In addition, Southeast Asian river sand is a major construction resource that is often unsustainably dredged and becoming increasingly scarce, resulting in bank erosion and collapse downstream and condemning low-lying river deltas to seawater intrusion and inundation (Xiqing et al., 2006; Kondolf et al., 2018; Best, 2019; Bendixen et al., 2019; Hackney et al., 2020). All together, damming, sand mining, and climate change will likely have a large impact on the Irrawaddy-Salween sediment fluxes, with negative consequences for downstream ecosystems and communities. It is therefore crucial to establish a baseline of the current sediment flux and composition, so that any impact from potential future environmental change can be accurately assessed.

2.2 Discharge measurements using ADCP

Flow velocity measurements and sediment samples of the Irrawaddy-Salween rivers were collected during two monsoon seasons, in August 2017 and 2018, and two dry seasons, in February 2018 and May 2019. Both rivers were sampled just upstream of their delta distributary networks (Fig. 1). Depth profiles of suspended sediments were collected each time, except in February 2018, when only surface samples were collected.

Flow velocity was measured using an Acoustic Doppler Current Profiler (ADCP) Rio Grande II (1200 kHz) made by Teledyne Instruments, deployed on a moving boat. The ADCP was attached on a rigid frame close to the bow, in a down-facing orientation, and the transducer submerged at 40-60 cm depth. Data were collected while the boat crossed the river perpendicular to the flow. Boat position during the transect was recorded using an external GPS unit with horizontal accuracy better than 5m. Between 1 and 5 such transects were collected, depending on the site, with discharge reproducibility typically better than 6%, in agreement with previous applications of moving-vessel ADCP (e.g., Szupiany et al., 2007).

ADCP data were collected and initially processed using WinRiver II software. The data were then exported and further processed using Velocity Mapping Toolbox (Parsons et al., 2013). Using multiple river cross-sectional transects, a mean cross-section (MCS) was created for each sampling date (Fig. 2), ensuring it was perpendic-

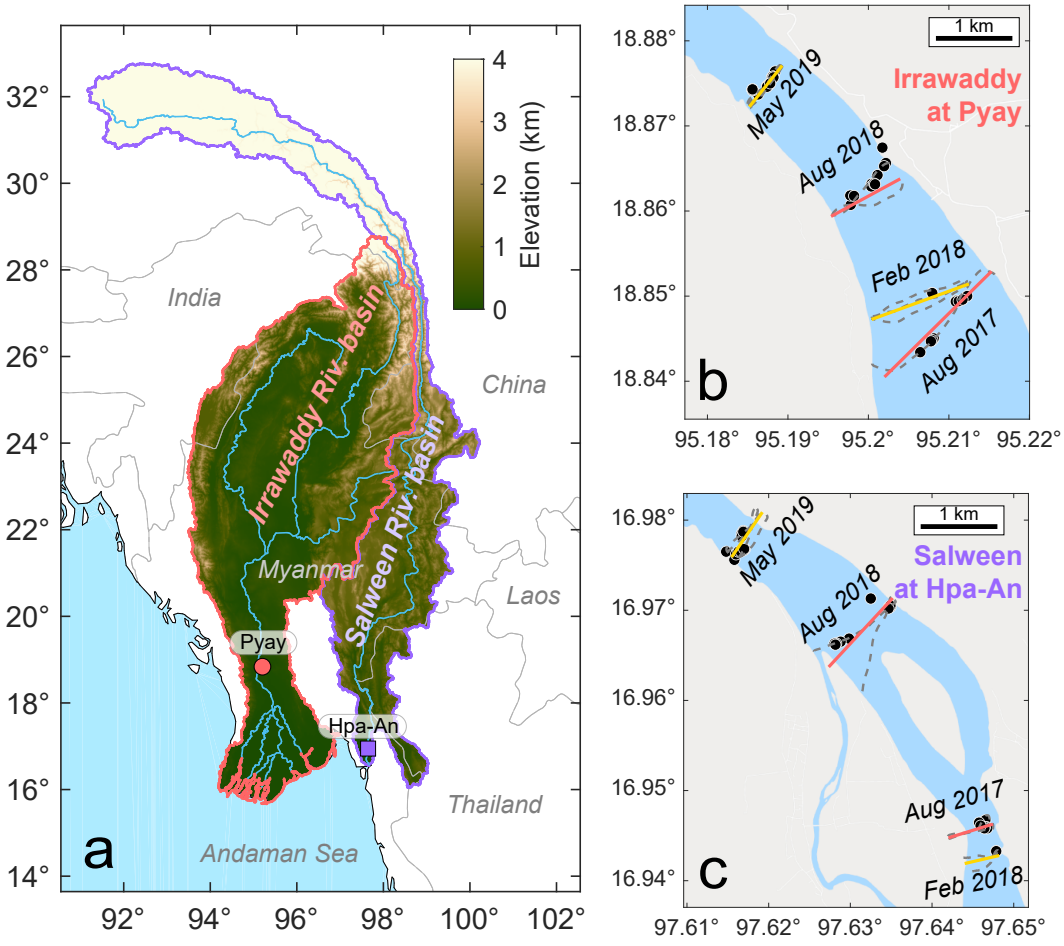

Figure 1. Map indicating the location of the study sites. a) Topographic map of the Irrawaddy and the Salween river basins, outlined in red and purple, respectively; country borders are shown as thin gray lines. The two sampling locations (Pyay on the Irrawaddy and Hpa-An on the Salween) are shown as a circle and a square, respectively. b, c) Detailed view of the ADCP transects (dashed gray lines) and the constructed mean cross sections (solid yellow and red lines) at each sampling location. Sediment depth sample locations are shown as black circles. Note that the exact channel course and width fluctuates seasonally and inter-annually and the channel shown in blue is an approximation.

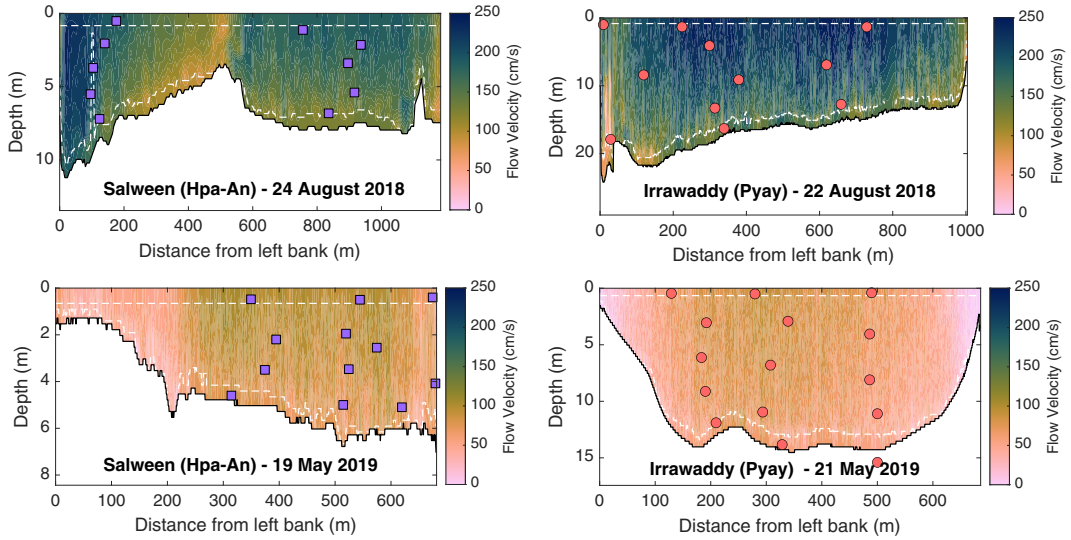

Figure 2. Examples of channel mean cross-sections (MCS) showing the water velocity distribution in the wet and the dry season at each site. Note the differences in axes scales of each panel. The squares and the circles show suspended sediment depth sample locations, projected flow-wise onto the MCS (see Fig. 1b-c for a top-down view of actual sampling locations). The white dashed lines show the regions where flow velocity data were extrapolated at the top (above ADCP transducer depth and blanking distance) and the bottom (below sidelobe interference) of each cross-section (see Section 2.2) .

ular to river channel, and calculating the average stream-wise flow velocity field across the river channel (Fig. 1b,c). The data were then additionally processed in MATLAB 2019b, interpolating data gaps and removing erroneous outlier data (e.g., due to excessive pitch and roll) and extrapolating to the river surface (above ADCP transducer) and bottom (below sidelobe interference) using *inpaint_nans* function (D'Errico, 2018).

2.3 Sediment sample collection and processing

Sediment samples were collected at various depths using a modified 8.5L capacity Van Dorn depth sampler (a Perspex acrylic tube open at both ends, with pneumatically triggered doors, modified from Wildco, USA). Depth was determined either from measured rope length (August 2017) or a pressure transducer (August 2018, May 2019). Approximately 30kg of metal weights (hammer heads) were attached below the sampler to ensure vertical position of the sampler relative to the boat. The samples were collected isokinetically, i.e. with the boat drifting with the flow. Once at the required depth, the sampler doors were pneumatically shut using a bicycle pump. Additional bedload samples were collected by dredging river bottom sediments using a weighted metal bucket.

Samples were collected into 10 L sterile polyethylene bags, ensuring complete transfer of all sediment particles. The bags were weighed and the samples filtered within 24h using 0.2 μm PES membrane. The sediments were immediately washed off the filter and into an opaque glass jar, using filtered river water collected at the same site. The samples were kept sealed in the dark during transport back to the lab (between 1 and 2 weeks). They were then allowed to settle and were decanted (except very clay-rich samples), followed by freeze-drying using a Thermo Scientific ModulyoD

freeze dryer. Suspended sediment concentration was calculated by dividing the dried sample weight by the weight of the total water sample prior to filtration, ignoring the <1% error due to sediment mass (<10g / kg) in the original sample.

Particle size distributions of dried samples were measured using a Malvern Mastersizer 2000 laser diffractometer, at a 20-bin resolution ranging between 0.35-2000 μm. Each sample amount was adjusted to achieve 10-20% obscuration and ranged from 50 to 5000 mg, depending on the coarseness. Each sample was dispersed in tap water and sonicated for 2-5 min until grain size distribution appeared stable. Each measurement was repeated 3-5 times. Typical uncertainty was better than 10% for each grain size bin, with most of the uncertainty due to subsampling errors of the coarse particles.

To measure the organic carbon concentration (weight %), carbonate was removed from the samples by a liquid HCl phase, within capsules with no rinse step (Komada et al., 2008). In detail, crushed sediment powders were weighed (approx. 5-10 mg sample for suspended sediments and 20 mg for bedload, attempting a target mass of organic carbon of ∼100 μg C) into 8 × 5 mm silver capsules that had previously been combusted (450 °C for 4 hours, within 3 days of processing) and loaded open into a PTFE sample tray. Around 50 μL of 1N HCl was added to each capsule, with the liquid reactant evaporated at 65 °C to dryness in an oven. Acid addition and drying was repeated three times in total. Capsules were folded close and analysed by EA-IRMS at Elemtex with a range of international calibration standards and external standards (IAEA 600, IAEA CH3) and to check for full carbonate removal (NCS-DC73319). Measured %OC values were corrected for a full procedural blank (<5% of the sample carbon mass) and repeat measurements of samples and external standards had a precision of 0.05%.

3 Revised hydrodynamic sediment transport model

River sediment is transported in suspension when turbulent shear stress (which can be expressed as shear velocity) is sufficient to overcome the particle settling velocity (e.g., Miller et al., 1977). Because turbulent shear stress affects all particles equally, whereas settling velocity depends on particle size, the ratio of these two parameters can theoretically predict how the concentration of particles of *a given size* would vary with depth (Rouse, 1950):

$$C_i(z_r) = C_0^i \cdot z_r^{R_i} \tag{1}$$

where

$$z_r = \frac{(H - z)/z}{(H - z_0)/z_0} \tag{2}$$

C_i is the sediment concentration in grain size class i and z_0 is a reference height, defined here as fixed fraction of total water depth $0.001 \cdot H$ (Lupker et al., 2011). The sediment concentration at this reference height is C_0^i. The "Rouse depth", z_r, is the sample depth z, non-dimensionalized relative to the reference height z_0 and total water column height H.

The power exponent in Eq. 1 is commonly referred to as the Rouse number:

$$R_i = \frac{w_i}{\beta \cdot \kappa \cdot u*} \tag{3}$$

The value of R_i is dependent on particle settling velocity w_i of sediment grain size i, the ratio of sediment and water momentum diffusion coefficients, β, and shear

velocity u^* (see Supp. Text Eq. S2); $\kappa = 0.41$ is the von Karman constant. The higher R_i, the stronger the increase in sediment concentration with depth.

Attempts to obtain R_i from fully theoretical considerations have so far been unsuccessful, due to a number of reasons. Firstly, it is difficult to accurately determine particle settling velocity, especially for natural sediments composed of mixtures of mineral and organic matter of variable density and shapes (Dietrich, 1982), with potential particle aggregation adding further complication (Bouchez, Métivier, et al., 2011). Secondly, while many simpler treatments take β to be equal to 1, experimental data have shown it to vary considerably with sediment concentration (Muste et al., 2005), likely the reason for the complex variations in β observed in real rivers (Lupker et al., 2011). For these reasons, previous workers were unable to apply Eq. 3 to large rivers, instead turning to empirical calibration of R_i using measured variations in sediment concentration with depth (Eq. 1) (Bouchez, Métivier, et al., 2011; Lupker et al., 2011).

In these previous applications of the Rouse model to large rivers, Eq. 1 was used to either obtain one average R_i across a river channel, effectively averaging laterally (Bouchez, Métivier, et al., 2011; Bouchez, Lupker, et al., 2011), or applied to depth profiles collected under varying hydrodynamic conditions and establishing an empirical fit between depth-averaged sediment flux and u^* (Lupker et al., 2011). In other words, Bouchez, Métivier, et al. (2011) and Bouchez, Lupker, et al. (2011) applied a single shear velocity value per cross-section, therefore only integrating the geometry of the channel to calculate the flux, without modeling the lateral variation in hydrodynamic conditions. This approach worked well for Bouchez et al. because they were modeling very deep (up to 60 m) river channels in relatively straight sections of the Amazon River and its major tributaries, where the lateral variation in shear velocity was minimal. This, however, is not the case for many rivers with more complex channel cross-section morphologies, such as the lower Irrawaddy and Salween rivers studied here (Fig. 2).

In contrast, Lupker et al. (2011) collected eight sediment sample depth profiles (n = 3-9 per profile) at the same site on the Ganges River, but under strongly varying hydrodynamic conditions over the course of several years. They then applied Eq. 1 individually to each depth profile, obtaining a vertically integrated sediment flux, relating it to local u^*, and then using this relationship to laterally and temporally extrapolate the vertically-integrated sediment flux. While robust, this approach requires a large number of suspended sediment samples and was enabled by a continuous field effort over the period of several years, and is therefore not ideal for the smaller sample set of our study.

Here, we employ a different approach from these previous studies to address the highly dynamic flow conditions of the rivers studied here, while using a smaller number of sediment depth samples. We do this by explicitly factoring u^* out of the fitted exponent in the Rouse equation:

$$C_i(z_r, u^*) = C_0^i \cdot z_r^{b_i/u^*} \tag{4}$$

where z_r is calculated from sample depth recorded during collection, u^* is calculated from the depth-integrated flow velocity during sample collection (see Supp. Text S1 for details), and C_0^i and b_i are fitted parameters (obtained separately for each grain size bin i).

Because b_i is strongly dependent on sediment grain size, and grain size distribution is known to vary widely with depth and hydrodynamic conditions in large rivers, measured sediment concentrations are divided into five grain size bins (i = 0.2-4, 4-16, 16-63, 63-250, 250-2000 μm) and Eq. 4 is then fitted individually to each one (Fig. 3;

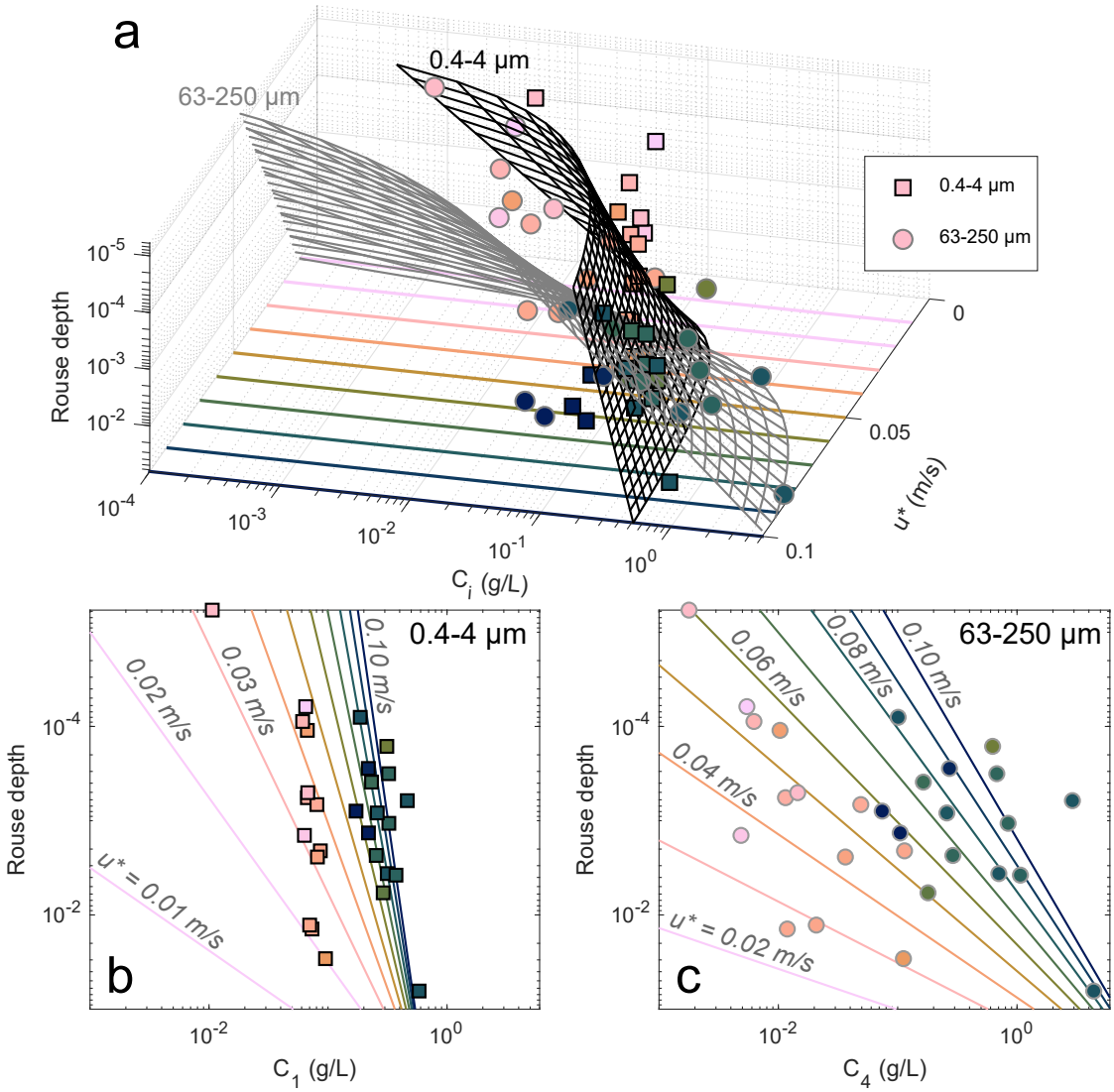

Figure 3. An example of three-dimensional fits to Eq. 4 (gridded curved surfaces in panel a) for two grain size fractions of measured Salween River suspended sediment concentrations (circles and squares). Rouse depth (z_r, as defined in Eq. 2) equals 1 at the river bed and 0 at the water surface. Panels b and c show the same fits and sample data in 2D representation separately for each grain size fraction. The colored lines in the bottom panels are projections (or "slices") of the three-dimensional gridded surfaces shown in (a) at selected u^* values, as indicated by the colored lines in (a). The sample symbols are also colored according to u^* associated with each sample (Supp. Table S1).

see Supp. Text S1). The empirically calibrated C_0^i and b_i values can then be applied to ADCP-measured velocity data to calculate and map high-resolution variations in sediment concentration C_i with depth and across the river channel (Fig. 4). Combining the five C_i values also yields the variation in sediment grain size across the channel (Fig.4). The suspended sediment flux $[kg\ m^{-2}\ s^{-1}]$ distribution across the channel is then calculated for each ADCP data bin as

$$q_s(z,x) = \sum_i C_i(z,x) \cdot u(z,x) \tag{5}$$

which can be summed up to obtain the total instantaneous suspended sediment flux $[kg\ s^{-1}]$:

$$Q_S = \sum_{z,x} q_s(z,x) \cdot A(z,x) \tag{6}$$

where z and x are the bin coordinates in vertical (depth) and horizontal (lateral distance across the channel) direction, respectively, u is flow velocity, and A is the cross-sectional area of a given ADCP bin (e.g., 0.25 m × 0.5 m).

In summary, the method described here has certain advantages over previous applications of the point sampling approach to integrate sediment variation with depth in large rivers:

1. Despite the additional degree of freedom (u^*) in the regression model (Eq. 4), it utilizes all sample data simultaneously (n = 30-37 in our case), rather than fitting sediment depth profiles one-by-one as done by Lupker et al. (2011) (n = 3-9), therefore improving the overall error minimization of the model fit to the data.
2. Because it relies on the Rouse equation, it does not require the explicit calibration of the ADCP sonar equation (Kostaschuk et al., 2005; Darby et al., 2016; Szupiany et al., 2019) and different ADCP instruments can be used to obtain flow velocity measurements during different field campaigns.
3. It enables a two-dimensional synoptic map of sediment concentration, flux, and grain size distribution across morphologically complex river channels, where depth and flow velocity often show significant lateral variations (Fig. 4) and where averaging across the channel (Bouchez, Lupker, et al., 2011; Morin et al., 2018; Santini et al., 2019) would likely result in significant errors of the calculated sediment flux and mean composition.

The above model applies only to sediment transported in suspension, and does not include sediment carried as bedload below the reference height z_0. To calculate the bedload flux, we adopted the semi-empirical bedload transport equation of van Rijn et al. (2007), as previously employed by Lupker et al. (2011), described in detail in Supp Text S2. The total instantaneous and time-averaged sediment flux values reported below are given as the sum of the suspended and the bedload sediment fluxes.

The sediment modeling procedure described above was applied to the Irrawaddy and the Salween rivers separately, calculating the mean sediment concentration, grain size, and %OC distribution, as well as the total instantaneous sediment and POC flux for each of the four ADCP cross-sections measured at each site. The results are summarized in Table 1 and the figures equivalent to Fig. 4 for the other seven cross-sections are given in the Supplementary Material.

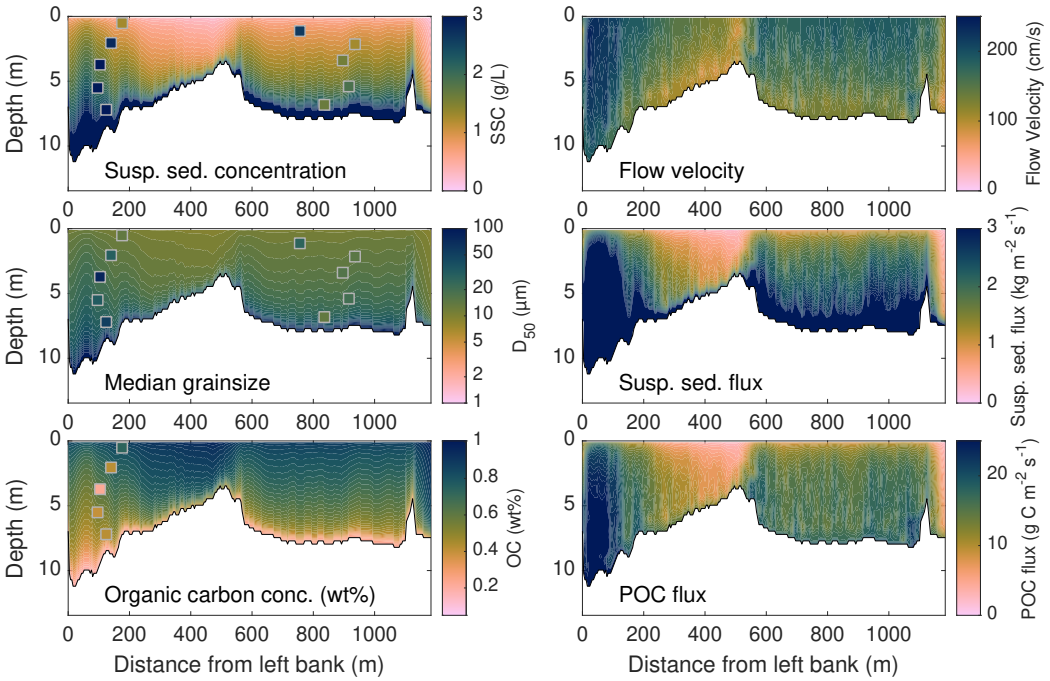

Figure 4. Results of the hydrodynamic sediment transport model for Salween at Hpa-An (2018 August 24), showing the depth and lateral variability in sediment composition and flux. The square colors reflect the measured sample compositions that were used to calibrate the model, demonstrating the model's ability to recover the initial values. Results for the other cross-sections are given in the Supp. Material.

Table 1. Measured instantaneous discharge and modeled sediment flux and composition of the Irrawaddy and Salween rivers.

River (site)	Date	Discharge (m^3/s) *	Sed. samples	Hydrodynamic model results						
				Sed. flux (kg/s)	Sed. flux (Mt/d)	Mean SSC (mg/L)	Mean D_{50} (μm)	Mean D_{84} (μm)	Mean OC (wt%)	POC flux (10^9 g C/d)
Irrawaddy (Pyay)	2017-08-23	42100	n = 10	56300 ± 5600	4.9 ± 0.5	1340 ± 130	41 ± 6	219 ± 22	0.23 ± 0.13	11.0 ± 1.1
	2018-02-03	3000	n = 1	720 ± 140	0.063 ± 0.013	240 ± 50	10 ± 1	71 ± 19	0.58 ± 0.15	0.36 ± 0.07
	2018-08-22	32100	n = 11	45500 ± 4430	3.9 ± 0.4	1360 ± 130	43 ± 6	228 ± 35	0.22 ± 0.13	8.7 ± 0.8
	2019-05-21	5300	n = 15	1490 ± 280	0.13 ± 0.02	280 ± 50	11 ± 1	93 ± 15	0.55 ± 0.14	0.70 ± 0.13
Salween (Hpa-An)	2017-08-21	11900	n = 7	25200 ± 2980	2.2 ± 0.3	2120 ± 250	32 ± 3	165 ± 7	0.46 ± 0.25	10.0 ± 1.2
	2018-02-01	1800	n = 1	400 ± 110	0.035 ± 0.009	230 ± 60	11 ± 1	37 ± 2	0.90 ± 0.30	0.31 ± 0.08
	2018-08-24	14300	n = 10	25200 ± 3060	2.2 ± 0.3	1760 ± 210	25 ± 2	136 ± 8	0.53 ± 0.26	12.0 ± 1.4
	2019-05-19	2700	n = 12	1230 ± 250	0.11 ± 0.02	460 ± 90	12 ± 1	41 ± 2	0.85 ± 0.29	0.9 ± 0.18

*Based on repeat transects, uncertainty better than 6% and in most cases better than 2%.

4 Results

The measured water discharge of the Irrawaddy and the Salween at each of the four sampling dates are given in Table 1. Measurements were performed at the peak of the monsoon season, as well as in mid- and late dry season, and therefore span about an order of magnitude range in discharge (3000-42100 m^3/s for the Irrawaddy and 1800-14300 m^3/s for the Salween). Importantly, these values bracket almost the full range of monthly mean discharge for both rivers (Supp. Table S4), allowing us to interpolate the results of this study for each month, yielding long-term average sediment composition and annual flux (see discussion below and Supp. Text S3).

The measured suspended sediment concentrations (SSC) ranged from 55 to 5500 mg/L in the Irrawaddy and 47 to 10200 mg/L in the Salween (all individual sample details and measured values are given in the Supp. Table S1). The median grain size (D_{50}) ranged from 5 to 150 μm in the Irrawaddy and 8 to 130 μm in the Salween. The most concentrated (and coarsest) samples were collected during the monsoon and typically closer to the channel bottom, indicating the influence of hydrodynamic sorting. However, a significant number of coarse, high-concentration samples in both rivers were collected at mid-depth (Fig. 5). Because our depth sampler collects instantaneous samples without time-averaging, the variable vertical dispersion of sand in our samples reflects the complexity of hydrodynamics in these rivers (e.g., non-steady state turbulent sediment suspension events, secondary flow, bedform effects, etc.). As discussed above, this complexity prevents simple spatial averaging with depth or across the river channel to calculate the total sediment flux and requires a fully spatially-resolved sediment transport model (Section 3).

To estimate the flux of particulate organic carbon (POC) by these rivers, we analysed the organic carbon concentration in a subset of the suspended sediment samples. As in many other rivers, in the Irrawaddy and Salween most organic carbon is associated with finer particles, and sediment OC (wt%) is closely correlated with median sediment grain size (Fig. 6). This relationship can be used to convert the spatial D_{50} distribution into %OC and subsequently, the POC flux (Fig. 4) can be calculated using equations equivalent to Eqs. 5 and 6.

5 Discussion

5.1 Instantaneous sediment flux and composition

The calculated total instantaneous sediment flux ranged from 700 to 56,000 kg/s and from 400 to 25,000 kg/s for the Irrawaddy and the Salween, respectively (Table 1).

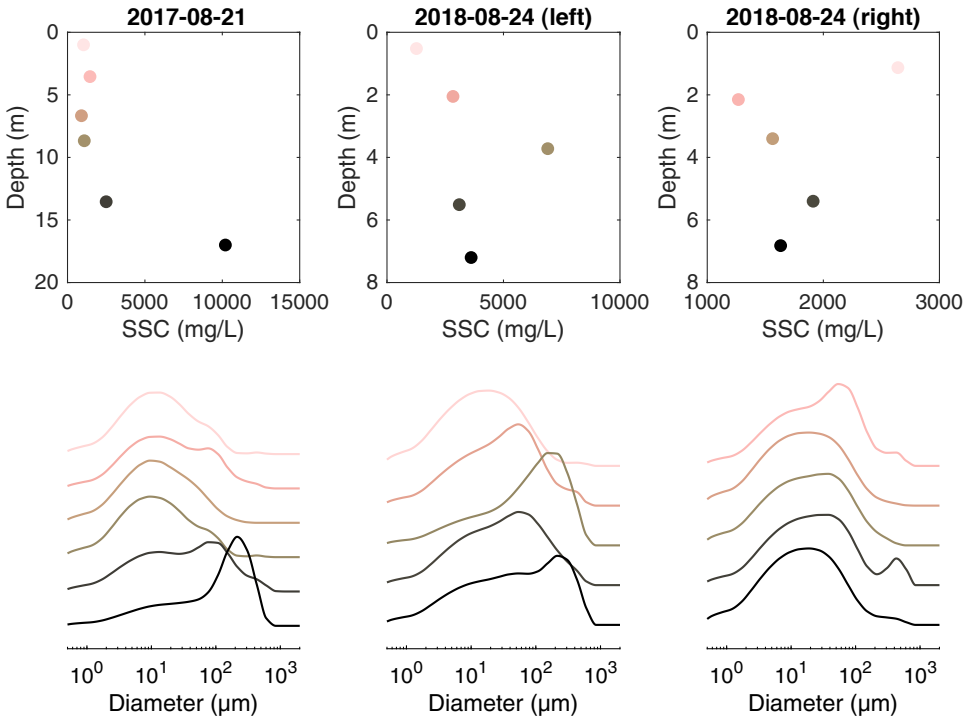

Figure 5. An example of measured variations in SSC (upper panels) and grain size distributions (lower panels, shown as relative probability density functions) with depth (darker colors reflecting deeper samples) at three locations across the Salween river channel during high discharge stage. The two profiles on 2018-08-24 correspond to the samples collected on the left and the right side of the channel, respectively, as shown in upper left panel of Fig. 2.

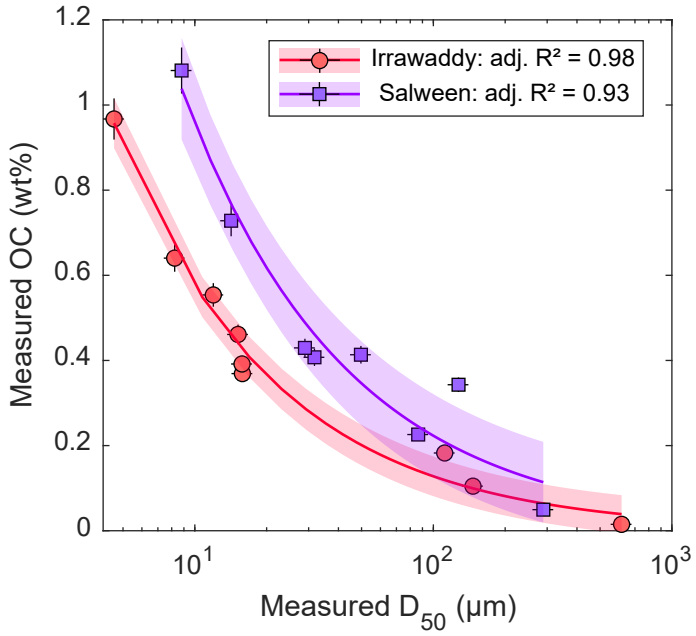

Figure 6. Relationship between measured sediment median grain size (D_{50}) and organic carbon content in each river, using samples collected across all seasons (incl. bedload). The dashed lines show power-law fits: $\%OC = (2.59 \pm 0.28)D_{50}^{(-0.65\pm0.05)}$ for Irrawaddy and $\%OC = (4.11 \pm 0.97)D_{50}^{(-0.63\pm0.08)}$ for Salween, with parameter uncertainties given as 68% confidence intervals.

The grain size distribution was generally coarser and more variable in the Irrawaddy (D_{50} range 10-43 μm) relative to the Salween (D_{50} range 11-32 μm). Although the Irrawaddy discharge and sediment flux is about 50% higher than the Salween, due to the higher %OC of Salween sediments, the POC fluxes were similar in both rivers, ranging from 0.3 to 12 $\cdot 10^9$ g C / day. The calculated bedload sediment flux ranged from 11 to 1500 kg/s in the Irrawaddy and 6 to 740 kg/s in the Salween, representing only 1-3% of the total sediment flux in each case, regardless of the hydrodynamic conditions. These results agree well with the similarly small portion ($\sim$1.5%) of total sediment flux carried in the bedload in the Ganges River (Lupker et al., 2011), as well as the Mekong River (Hackney et al., 2020), both similar in size to the Irrawaddy in their lower reaches. The total instantaneous (Table 1), monthly (Fig. 7; Supp. Table S4), and annual (Table 2) sediment flux values are all given as the sum of the suspended and the bedload sediment fluxes. The bedload POC flux is ignored, given that coarse sand contains low %OC (Fig. 6) and that the majority of sediment is carried as suspended load, this approximation should result in a negligible underestimation of the total POC flux.

5.1.1 The performance of the hydrodynamic sediment transport model

To assess the performance of the model, the measured sample compositions can be compared to values calculated using the model at the equivalent locations (depth and lateral) in each channel cross-section. An example of a visual comparison between the measured and calculated parameters for the Salween in August 2018 is given in Fig. 4, with other cross-sections shown in Supp. Material. A more detailed comparison is shown for all sediment samples at both sites in Fig. 8. The degree of misfit between measured and modeled values (represented as a mean relative standard error) was less than 5% for SSC and D_{50} in both rivers, while the %OC relative standard error was -35% for the Irrawaddy and +30% for the Salween. The higher and more systematic misfit of %OC is likely due to the considerably smaller number of data available to calibrate the model (Figs. 6, 8c) compared to SSC and D_{50} and should be improved with additional analyses. We also note that this is not a strict test of the model, as it uses the training dataset to assess the performance. A more rigorous assessment can be performed in the future against similar additional datasets (i.e., sediment samples coupled to ADCP flow velocity measurements) at these sites.

We propose that there are three main reasons for the misfit between the modeled and the measured values:

1. In some cases, large deviations from expected sediment sorting were observed, with several coarse, high-SSC samples collected at mid-depth (Fig. 5), likely due to non-steady state suspension events during sampling as discussed above.
2. There is some degree of mismatch between the ADCP velocity measurements (which integrate over a increasingly larger horizontal area with increasing depth) and the exact location of the collected sediment samples.
3. The location and the shape of the channel cross-section varied slightly from year to year at both sites (Fig. 1b,c; Supp. Figures).

These factors inject substantial noise into our sample set, resulting in an offset between the sampled sediments and the local hydrodynamic conditions (represented by shear velocity) assigned to each sample (see Supp. Text S1). Finally, an additional source of uncertainty is the possible change in sediment supply to each river (e.g., seasonal hysteresis, or inter-annual variations caused by landsliding or land-use changes upstream) during the time-span over which samples were collected for this study. However, such effects are typically local and we expect them to be minor compared to the immediate turbulence-induced noise (point no. 1 above), and to be mostly

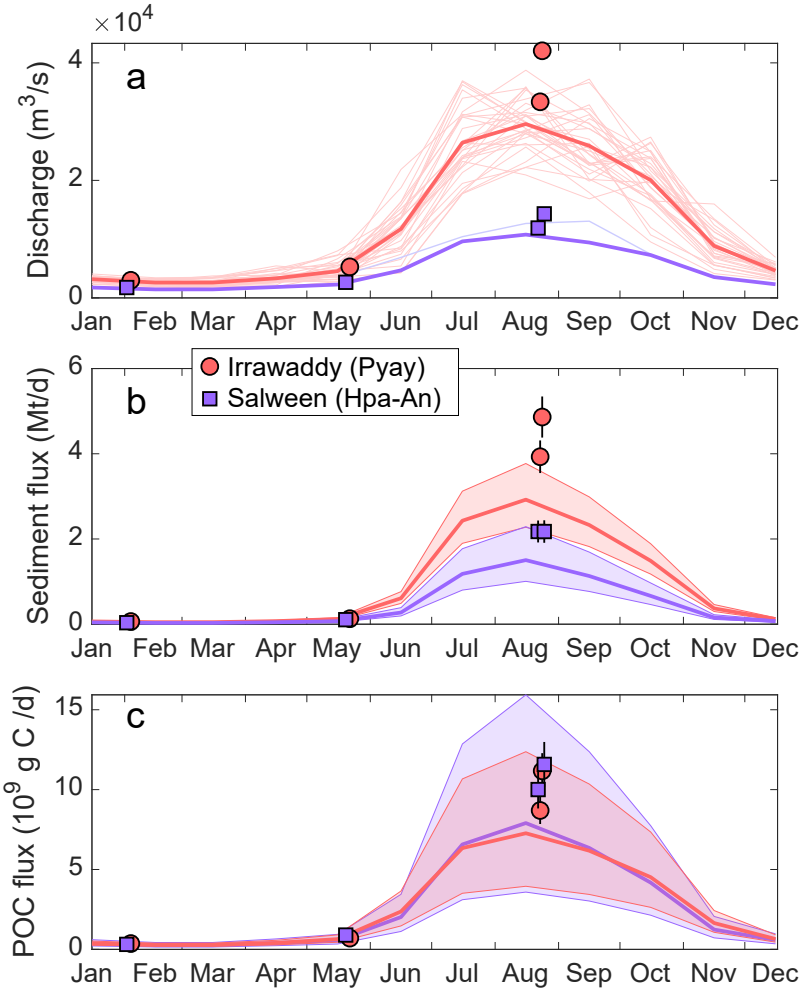

Figure 7. Average monthly discharge (a), sediment (b), and particulate organic carbon (c) fluxes in the Irrawaddy and Salween rivers. Our ADCP-measured discharge and Rouse-calculated flux values are shown as circles and squares for the Irrawaddy and Salween, respectively (see Section 5.1.1). Thin lines in (a) show discharge data reported by the Department of Hydrology and Meteorology in Myanmar (1966-1996 for the Irrawaddy; May-Oct 2004 for the Salween, previously published by Furuichi et al. (2009) and Chapman et al. (2015), respectively). For discharge, the thick line represents the 31-year monthly averages for the Irrawaddy, whereas the Salween monthly discharge was calculated using the Irrawaddy/Salween discharge ratio determined in the wet and dry seasons in this study (see Supp. Text S3 for details). In (b) and (c), the thick line shows the best estimate with shaded area as the 68% confidence interval propagated through all calculations (see Supp. Text S3).

averaged out on the large basin-scale considered here. Ultimately, the spatial distribution of sampled sediment composition cannot be fully reconciled using a model that implicitly assumes constant sediment supply, constant channel structure, and equilibrium hydrodynamic conditions. Despite these complications, the sediment transport model presented here recovers the initial sample sediment composition for both the Irrawaddy and the Salween, without any large systematic errors (Fig. 8). The relative standard error (i.e., the mean residual of measured vs. modeled values) was better than $\pm 5\%$ for both SSC and D_{50} (Fig. 8a-b) and was -35% for %OC in the Irrawaddy and +30% in the Salween (Fig. 8c), likely due the smaller number of available data and error propagation in the $D_{50} - \%OC$ calibration (Fig. 6). The utility and need for such a model is further evaluated below, by comparing the flux and mean sediment composition values calculated here with estimates derived using simpler approaches.

Table 2. Properties of the river basins and the mean annual sediment composition and fluxes calculated in this study (see text). Except for elevation, the calculated values in parentheses represent a 68% confidence interval. The elevation and median slope were determined using the hydrologically conditioned MERIT HYDRO digital elevation model (Yamazaki et al., 2019).

	Irrawaddy	**Salween**	
Basin properties			*units*
Planimetric area	422,400	266,500	km^2
DEM surface area [a]	436,500	282,300	km^2
Mean elevation (range)	862 (0-5790)	3515 (0-6860)	*m*
Median slope	7.1	16.4	*degrees*
Geology	Marine silic. sedim., some metamorphic and igneous rocks; large central alluvial valley	Mixed limestones, granitoids, and metamorphic rocks	
Results [b]			
ADCP discharge measurements	n = 4	n = 4	
Susp. sed. samples	n = 37	n = 30	
Water discharge [c]	379 ± 9	149	$km^3\ yr^{-1}$
Runoff [d]	900 ± 20	560	$mm\ yr^{-1}$
Sed. flux	326 (256-417)	159 (109-237)	$Mt\ yr^{-1}$
POC flux	0.95 (0.55-1.55)	0.94 (0.46-1.79)	$Mt\ C\ yr^{-1}$
Erosion rate [e]	0.28 (0.22-0.35)	0.21 (0.14-0.31)	$mm\ yr^{-1}$
Sed. yield [e]	750 (590-960)	560 (390-840)	$t\ km^{-2}\ yr^{-1}$
POC yield [e]	2.2 ± 1.2	3.3 (1.6-6.3)	$t\ C\ km^{-2}\ yr^{-1}$
Mean SSC	0.9 (0.7-1.1)	1.1 (0.7-1.6)	$g\ L^{-1}$
Mean D_{50}	28 (23-34)	21 (17-26)	*μm*
Mean D_{84}	183 ± 13	112 ± 27	*μm*
Mean OC	0.29 ± 0.08	0.59 ± 0.16	*wt%*

[a] Based on MERIT HYDRO DEM (Yamazaki et al., 2019), down-sampeld to 90m resolution.

[b] See Supp. Text for details of calculations.

[c] Using previously published data from the Department of Meteorology and Hydrology in Myanmar (see Supp. Text).

[d] Calculated using planimetric area.

[e] Calculated using DEM surface area.

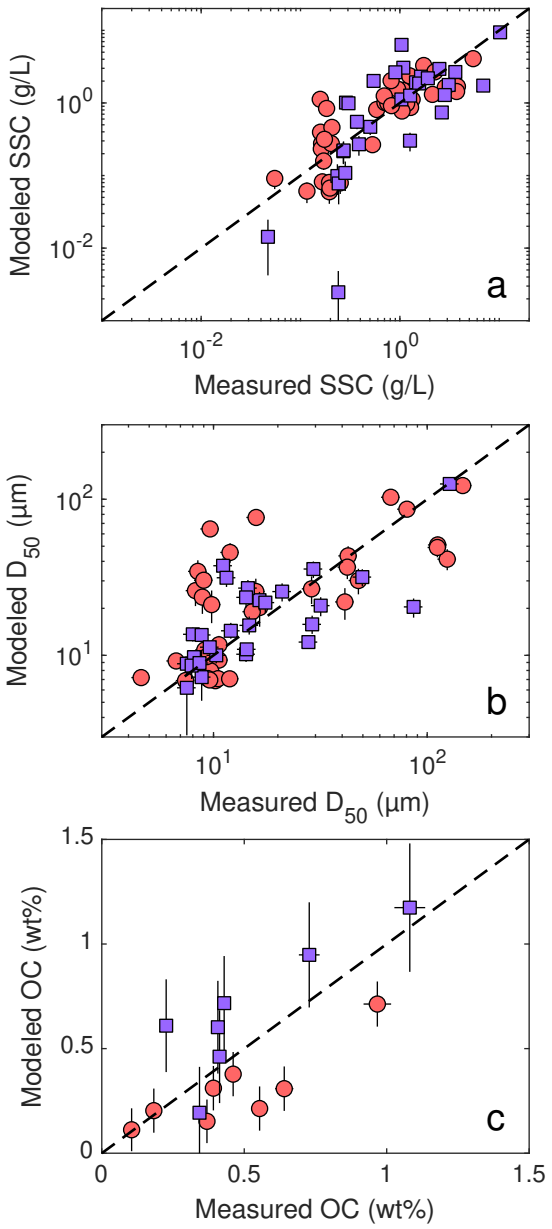

Figure 8. Comparison of measured sediment composition with values re-calculated using the sediment transport model described in Section 3 for all Irrawaddy (red circles) and Salween (purple squares) River samples. Dashed lines show 1:1 relationship. The horizontal error bars represent analytical uncertainty, while the vertical error bars were calculated using a 68% confidence interval of the Rouse model fit (Eq. 4; Fig. 3). Measured and recalculated values for all samples are given in the Supp. Table S1.

5.1.2 The need for a hydrodynamic sediment transport model

Our results indicate that, at least in the case of the Irrawaddy and the Salween, the sampled sediments frequently deviate from the expect Rousean behaviour, that is, sampled sand concentration does not always increase with depth (Fig. 5). It is therefore reasonable to ask whether a Rouse-based hydrodynamic sediment transport model is required, and whether a simple averaging of all sediment samples, such as employed previously by Robinson et al. (2007) for the Irrawaddy, would yield flux and mean sediment composition estimates that are indistinguishable from the more complex hydrodynamic modeling approach employed in this study. A comparison of the instantaneous sediment and POC fluxes, as well as mean grain size parameters calculated using the different approaches (including previously published rating curves and %OC values) is shown in Table 3. Given that we collected sediment samples at roughly consistent depth percentiles (typically 5-25-50-75-95% or 5-50-95% of total depth), as well as at several different lateral locations across the channel, we consider our sample set to be reasonably uniform in both dimensions of the channel cross-section. Taking a simple average of the sampled SSC values and multiplying by the total ADCP-measured discharge has yielded sediment flux estimates that ranged from ∼40% lower during the dry season to ∼50% higher during the wet season, compared to Rouse model results for both rivers. Similarly, the mean grain size parameters (D_{50} and D_{84}) were frequently over- or under-estimated, depending on the particular cross-section, reflecting the fact that simple-mean estimates fail to accurately account for sand transport in the near-bed region. Finally, using simple means of measured values significantly overestimated the POC flux by anywhere between 40 and 95% during the wet season for both rivers. Given the large size and discharge of the two rivers, this would result in a non-negligible error of riverine carbon export on a globally relevant scale. This comparison shows how crucial it is to accurately account for hydrodynamic sorting of sediments in large and morphologically and hydrodynamically complex rivers.

Although the chemical composition of the transported sediments is outside of the scope of this study, similar averaging errors can significantly affect the calculated fluxes of chemical elements which are highly sensitive to particle grain size, such as silicon (mostly contained in coarser quartz sand grains) and aluminum and iron (mostly contained in clay particles). These sorting bias effects were well exemplified and quantified on an element-by-element basis by Bouchez, Gaillardet, et al. (2011) and Lupker et al. (2011) for the Amazon and the Ganges rivers, respectively. Given the importance of hydrodynamic sorting for the SSC and POC values in the Irrawaddy and Salween, we therefore expect similarly significant bias in elemental (and isotopic) fluxes, to be explored in follow up studies.

5.2 Temporal integration of sediment flux and composition

The mean SSC and POC values calculated at the four different sampling dates and discharge (Q_w) conditions for each river allowed SSC-Q_w rating curves to be constructed (Fig. 9). Using previously published monthly Irrawaddy discharge data over a 31-year period (1966-1996) (Furuichi et al., 2009), we can calculate the monthly sediment and POC fluxes (Fig. 7) and mean sediment concentration, grain size, and organic carbon content (Fig. 10), which can then be summed to obtain long-term average annual values, summarized in Table 2. Unfortunately, other than our measurements presented here, the only Salween discharge data available cover a period between May-Oct in 2004, previously published by Chapman et al. (2015). The only annual discharge value available for the Salween is 210 km^3/y given by Meybeck and Ragu (1997), which has since been used in a number of publications on rivers in Myanmar, as well as global compilations of water, sediment, and chemical fluxes (e.g., Gaillardet et al., 1999; Robinson et al., 2007; Chapman et al., 2015). For this reason,

Table 3. Comparison of hydrodynamic Rouse-based model results with simple mean-derived estimates using the sample set presented here, as well as previously published fluxes (Robinson et al., 2007; Bird et al., 2008).

Date	Parameter	Previous estimate [a]	Simple mean [b]	Rouse model [c]	Error [d]
Irrawaddy (Pyay)					
2017-08-23	Total sed. flux (Mt/d)	3.5	7.4	**4.9**	52%
2018-02-03		0.06	0.04	**0.06**	-31%
2018-08-22		2.3	3.4	**3.9**	-13%
2019-05-21		0.14	0.08	**0.13**	-36%
2017-08-23	POC flux (kg/s)	470	218	**129**	69%
2018-02-03		11	--	**4**	--
2018-08-22		308	157	**97**	62%
2019-05-21		26	--	**8**	--
2017-08-23	D_{50} (µm)	--	65	**41**	60%
2018-02-03		--	--	**10**	--
2018-08-22		--	23	**43**	-46%
2019-05-21		--	10	**11**	-11%
2017-08-23	D_{84} (µm)	--	216	**219**	-1%
2018-02-03		--	--	**71**	--
2018-08-22		--	134	**228**	-42%
2019-05-21		--	27	**93**	-71%
Salween (Hpa-An)					
2017-08-21	Total sed. flux (Mt/d)	--	2.1	**2.2**	-2%
2018-02-01		--	0.02	**0.03**	-38%
2018-08-24		--	3.3	**2.2**	52%
2019-05-19		--	0.08	**0.11**	-29%
2017-08-21	POC flux (kg/s)	227	226	**116**	95%
2018-02-01		26	--	**4**	--
2018-08-24		227	185	**134**	38%
2019-05-19		26	--	**11**	--
2017-08-21	D_{50} (µm)	--	35	**32**	9%
2018-02-01		--	--	**11**	--
2018-08-24		--	31	**25**	21%
2019-05-19		--	9	**12**	-23%
2017-08-21	D_{84} (µm)	--	105	**165**	-37%
2018-02-01		--	--	**37**	--
2018-08-24		--	114	**136**	-17%
2019-05-19		--	43	**41**	5%

[a] Sediment and POC fluxes recalculated for instantaneous discharges measured in this study (Table 1), using the SSC rating curve determined by Robinson et al. (2007) and the season-average wt% OC determined by Bird et al. (2008)

[b] Calculated as product of discharge and a simple mean of SSC and POC for all samples collected and analyzed on a given date, where n > 1 (Table S1).

[c] Calculated using the Rouse modelling approach described in Section 3.

[d] Calculated as the relative difference between the simple mean-calculated value and the Rouse model-calculated value.

we used our ADCP-measured discharge values, along with the average monthly Irrawaddy discharge, to re-estimate the monthly discharge of the Salween in proportion to Irrawaddy discharge, yielding a revised annual Salween discharge of 149 km^3/y (see Supp. Text S3 for details).

Applying the rating curves shown in Fig. 9 to the monthly discharge timeseries, we are able to calculate the monthly suspended sediment and particulate organic carbon concentrations, median grain size (Fig. 10) and the sediment and POC fluxes (Fig. 7; all values given in Supp. Table S4). As expected, the sediment composition and flux varies by more than an order of magnitude in both rivers, with the coarsening of the transported sediment and the highest fluxes during the monsoon: monthly mean SSC ranged from 0.20 to 1.1 g/L in the Irrawaddy and from 0.22 to 1.6 g/L in the Salween, with annual flux-weighted means of 0.9 ± 0.2 and $1.1^{+0.5}_{-0.4}$ g/L, respectively (1σ uncertainty; Table 2). Overall, the Salween sediments are finer (D_{50} from 11 to 25 μm, compared to the Irrawaddy's 10 to 42 μm, with flux-weighted annual means of 21^{+5}_{-4} and 28^{+6}_{-5} μm, respectively.

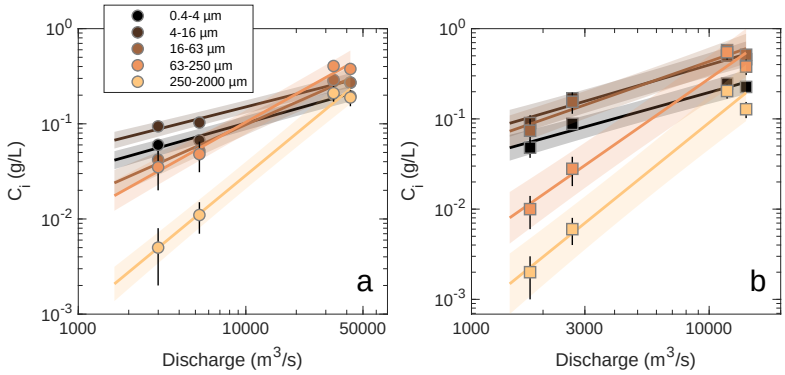

Figure 9. Rating curves used to calculate monthly and annual sediment average composition and flux for the Irrawaddy River at Pyay (a) and the Salween River at Hpa-An (b). The symbols show the mean suspended sediment concentrations calculated using the hydrodynamic sediment transport model, for five different grain size fractions (Section 3, Table 1). The lines and envelopes show best fit and 68% confidence interval of the fit. The fitted rating curves and the goodness-of-fit statistics are given in Supp. Materials.

Due to its lower discharge, the Salween sediment flux of 159^{+78}_{-51} Mt/y is about half of the Irrawaddy's 326^{+91}_{-70} Mt/y, with bedload comprising ~2% of each. However, because organic carbon concentration in the Salween is about twice that of the Irrawaddy (0.59±0.13 vs. 0.29±0.08 %), both rivers deliver a similar POC flux of ~1 Mt C/yr to the ocean.

5.3 Comparison to previously published annual flux estimates

Compared to other major global rivers, prior to this study there existed very little modern data on the water and sediment discharge in the Irrawaddy and the Salween. The most significant dataset was published in the 19th century by Gordon (1880), presenting 10 years of discharge and suspended sediment measurements on the Irrawaddy at a location close to our sampling site at Pyay. More recently, Robinson et al. (2007) collected additional sediment depth samples and re-evaluated the original Gordon dataset, determining annual estimates of water discharge of 422±41 km^3/y

and sediment flux of 364±64 Mt/y. Subsequently, Furuichi et al. (2009) used 31 years of discharge data published by the Department of Hydrology and Meteorology (DHM) in Myanmar (the same dataset was used in this study) to calculate annual discharge of 379±47 km^3/y, where the uncertainty was given as 1 standard deviation of inter-annual variability and is therefore an overestimate of actual uncertainty on the long-term average, which we recalculate here as 1 standard error of the mean, equal to 9 km^3/y (Table 2) for the same 31 year period. Furuichi et al. (2009) further used a sediment rating curve for the Irrawaddy developed by DHM to estimate an annual sediment flux of 325±57 Mt/y, in good agreement with our results. However, it must be noted that neither the sampling protocol nor the data used to establish the rating curve given in Furuichi et al. (2009) are publicly available.

Similarly, we revised the Salween sediment flux from 180 Mt/y previously estimated by Robinson et al. (2007) using the Irrawaddy sediment rating curve, down to 159^{+78}_{-51} Mt/y, using the first rating curve for the Salween, presented here. We note that discharge monitoring of the Salween is necessary to further improve this estimate.

Finally, our determined annual POC fluxes are significantly lower than the values previously presented in Bird et al. (2008): 0.55-1.55 vs. 2.2-4.3 Mt C/y for the Irrawaddy and 0.46-1.79 vs. 2.4-3.4 Mt C/y for the Salween, a two-to-five-fold reduction in each case. It is partly explained by the reduction in water discharge estimates but the main reason appears to be significantly lower %OC measured in this study (Table 2, also see Supp. Material for individual sample values), compared to the values determined by Bird et al. (2008). One possibility is that this difference represents an actual decrease in %OC over the past decade. However, a change of this magnitude is difficult to defend, considering the large area of both river basins, and the fact that the difference is of similar order for both rivers. We suggest that this discrepancy is likely the result of sampling methodology differences between Bird et al. (2008) and the present study. Bird et al. (2008) used a 2L horizontal Van Dorn sampler, collecting sediment samples at 1 m depth from the surface, mid-depth, and 1 m depth from the bottom, measuring OC of 1.1-1.6 wt% during high-discharge monsoon conditions, with similar values in both Irrawaddy (at Pyay) and Salween (at Hpa-An) and almost constant throughout the water column, suggesting negligible hydrodynamic sorting. This observation is in stark disagreement with both the results presented in this study, as well as the similar increase in SSC with depth observed by Gordon (1880). Although it is difficult to determine the exact reason for this discrepancy, we speculate that sand may not have been adequately sampled by the smaller 2L volume sampler used by Bird et al. (2008) (vs. our 8.5L sampler, where we took extreme care to rinse out and collect all sand particles during sample transfer). This reinforces why thorough depth sampling and sediment flux modeling that accounts for hydrodynamic sorting is crucial for accurate flux estimates in large rivers, especially for elements such as carbon, whose concentrations are strongly coupled to sediment grain size (Fig. 6).

5.4 Global significance of the Irrawaddy-Salween system

Globally, using the values presented in this study, the Irrawaddy and the Salween exhibit some of the highest sediment fluxes (fifth and seventh worldwide, respectively; Fig 11) and area-normalized sediment yields (third and fourth, respectively, among world's 30 major global rivers with annual discharge $> 100\ km^3\ y^{-1}$ as compiled by Milliman and Farnsworth (2011), and lower only than the Fly and Brahmaputra rivers). Compared to the nearby Ganges-Brahmaputra system, which is the main conveyor of Himalayan erosion products to the ocean, the Irrawaddy-Salween system sediment yield is very similar and sediment flux is about 46% that of Ganges-Brahmaputra. In comparison, the Mekong River, also originating in the eastern Himalayan Syntaxis, used to deliver ∼150 $Mt\ y^{-1}$ (Milliman & Farnsworth, 2011), which has decreased to $87 \pm 28\ Mt\ y^{-1}$ (∼2 and ∼4 lower than the current fluxes of the Salween and the

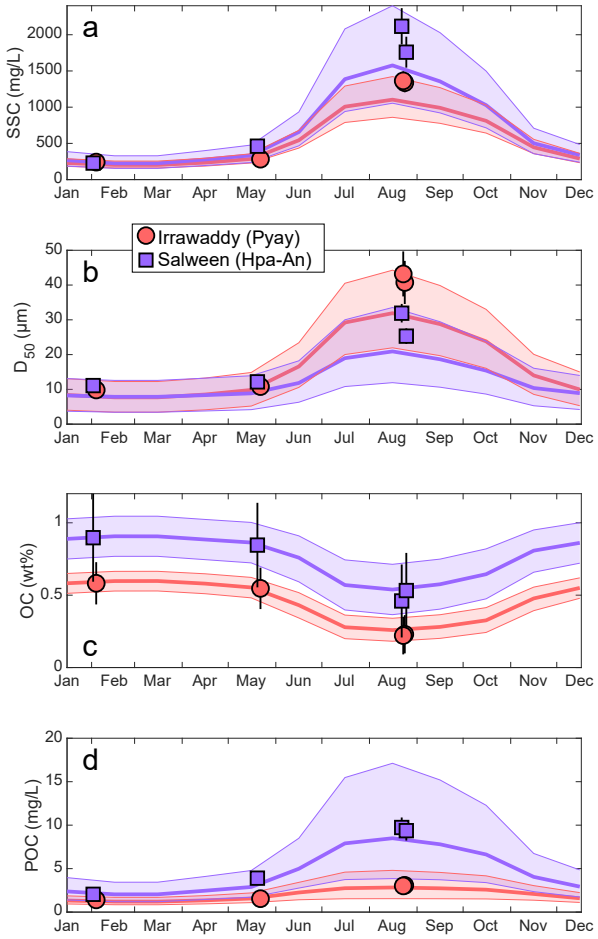

Figure 10. Average monthly SSC (a), median grain size D_{50} (b), organic carbon wt% (c), and POC concentration (d) in the Irrawaddy and Salween rivers. Our model-calculated flux values that were used to construct rating curves are shown as circles and squares for the Irrawaddy and Salween, respectively (see Section 5.1.1, Table 1). The thick line shows the best estimate with a 1σ uncertainty indicated by the envelope. Details of calculations are given in Section 5.2 and Supp. Text S3 and the calculated monthly values are given in Supplementary Material.

Irrawaddy, respectively) over the past several decades due to damming and changes in precipitation across the basin (Darby et al., 2016).

Although it is difficult to assess the global significance of the Irrawaddy-Salween system due to uncertainty of the global sediment flux, comparing to the estimate of Milliman and Farnsworth (2011), the two rivers are an important source of sediment to the ocean, delivering 2-3% of the 19,000 $Mt\ y^{-1}$ total sediment and 0.8-1.2% of the 200 $Mt\ C\ y^{-1}$ total (biospheric and petrogenic) POC (Galy et al., 2015) export to the ocean. It must be noted, however, that current sediment flux estimates may be inaccurate for a number of large global rivers, where values are derived from sparse sample sets, often of surface sediments only, lacking the depth sampling and hydrodynamic data required to obtain robust values. The significance of our results is further underlined by the fact that the Irrawaddy and the Salween are some of the last large

rivers basins still relatively unaffected by damming. Only a few small dams have been built on some minor tributaries of both rivers, with their mainstems flowing freely from source to outlet (worldwide, the only other megarivers with free-flowing mainstems are the Amazon and the Congo; Grill et al. (2019)). Currently, the main anthropogenic pressures on these river basins, such as deforestation, agriculture, and sand mining, are likely to be net erosive, enhancing the sediment flux (Syvitski et al., 2005). However, large dams are planned on both rivers, which, if built, will trap large amounts of sediment, strongly reducing the net export to the deltas. Our results presented here thus establish an important pre-dam baseline of sediment export by the Irrawaddy-Salween system.

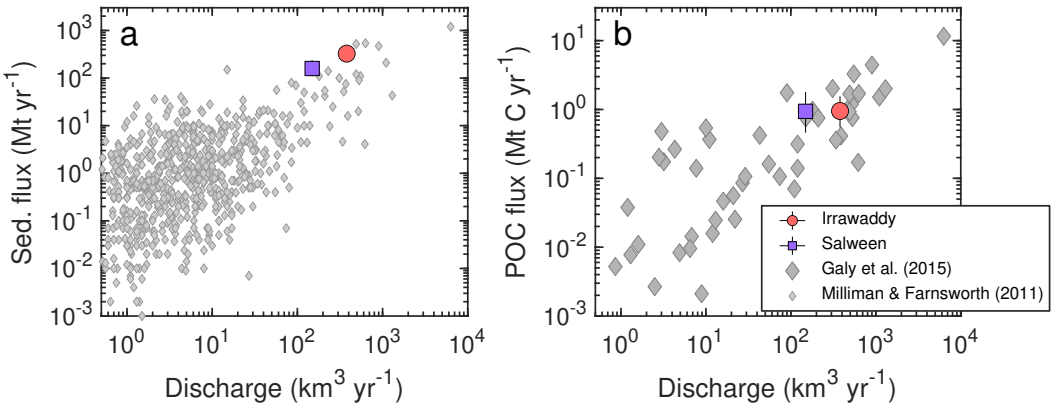

Figure 11. Comparison of the Irrawaddy and Salween (a) total sediment and (b) POC fluxes to other major global rivers.

6 Conclusions

In this contribution, we have presented a new semi-empirical hydrodynamic Rouse modeling approach to synoptically predict the two dimensional distribution suspended sediment concentration, physicochemical composition (grain size and organic carbon content), and flux in large, turbulent rivers with geomorophologically complex channels. We have applied this model to obtain spatially- and temporally-integrated estimates of the sediment composition and export flux of the Irrawaddy and Salween rivers in Southeast Asia. In comparison to the model, flux estimates derived from using simple means of evenly-spaced depth point samples can result in errors of up to 50%. This demonstrates that synoptic (i.e. spatially highly-resolved) sediment transport modeling is crucial for the accurate quantification of sediment composition and flux in large river channels, where wide sediment grain size distributions and variable hydraulic conditions result in complex sediment transport patterns.

Using the approach outlined above, we have calculated a total sediment flux of 485 (68% confidence interval of 364-654) Mt/yr and a particular carbon flux of 1.9 (1.0-3.3) Mt C/yr for the Irrawaddy-Salween system, accounting respectively for 2-3% and 0.8-1.2% of the total global riverine export to the ocean. These new estimates represent a ∼20% and a 60-80% reduction of sediment and POC fluxes, respectively, compared to previously best estimates, which were partly based on 19th century data. While some of this difference may potentially be accounted for by actual changes in deforestation, land-use, and other anthropogenic pressures in the river basins, we suggest that most of the difference is likely methodological, stemming from the use of a robust hydrodynamic sediment transport model in the current study. We expect that

the methods and results described here, when combined with chemical and isotopic analyses of sediments at these and other sites in the Irrawaddy and the Salween basins, will enable a deeper understanding of the sediment provenance, erosion, and chemical weathering dynamics in the region, with the ultimate aim of fully constraining the regional organic and inorganic carbon cycle.

While the upstream sediment supply remains relatively constant, our calibrated Rouse-model fits presented here allow the use of ADCP data to predict the spatial distribution of SSC and POC across each river channel in the future. In turn, our calibrated SSC rating curves allow the prediction of total sediment flux with varying discharge. However, given that a number of large dams are planned on major tributaries and mainstems of both rivers, sediment supply to their respective lower basins are expected to change, if and once these dams are constructed. In this case, active, depth-sampling based monitoring of sediment fluxes will be required to accurately quantify the changing sediment flux and composition. In this case, the results of our current study provide an important pre-dam baseline against which future changes can be evaluated.

Acknowledgments
All measurement and final model results are tabulated in the main text and in the Supplementary Tables. Raw and processed ADCP data files and individual cross-section model results are available on PANGAEA data repository (*author note: will be uploaded and hyperlink included here upon acceptance*). Funding was provided by NERC Standard Grant NE/P011659/1 to ETT, RJH, and MJB. We thank Si Thu, Charlie Eardley, Vivian Cummings, Luke Bridgestock, Hazel Chapman, and staff of DWIR for help in the field. Tamsin O'Connell and Catherine Kneale (Dept. of Archaeology, U. of Cambridge) are thanked for assisting with freeze drying. Olly Dawes and Laura Healy helped with sediment grain size analyses at the University of Hull and the University of Cambridge, respectively.

References

Allison, M. a., Bianchi, T. S., McKee, B. a., & Sampere, T. P. (2007, 1). Carbon burial on river-dominated continental shelves: Impact of historical changes in sediment loading adjacent to the Mississippi River. *Geophysical Research Letters*, *34*, L01606. Retrieved from `http://doi.wiley.com/10.1029/2006GL028362` doi: 10.1029/2006GL028362

Armijos, E., Crave, A., Espinoza, R., Fraizy, P., Santos, A. L., Sampaio, F., ... Filizola, N. (2017). Measuring and modeling vertical gradients in suspended sediments in the Solimões/Amazon River. *Hydrological Processes*, *31*(3), 654–667. doi: 10.1002/hyp.11059

Bendixen, M., Best, J., Hackney, C., & Iversen, L. L. (2019, 7). Time is running out for sand. *Nature*, *571*(7763), 29–31. Retrieved from `http://www.nature.com/articles/d41586-019-02042-4` doi: 10.1038/d41586-019-02042-4

Berner, R. A., & Kothavala, Z. (2001). Geocarb III: A revised model of atmospheric CO2 over phanerozoic time. *American Journal of Science*, *301*(2), 182–204. doi: 10.2475/ajs.301.2.182

Best, J. (2019, 1). Anthropogenic stresses on the world's big rivers. *Nature Geoscience*, *12*(1), 7–21. Retrieved from `http://dx.doi.org/10.1038/s41561-018-0262-xhttp://www.nature.com/articles/s41561-018-0262-x` doi: 10.1038/s41561-018-0262-x

Bird, M., Robinson, R., Win Oo, N., Maung Aye, M., Lu, X., Higgitt, D., ... Hoey, T. (2008, 8). A preliminary estimate of organic carbon transport by the Ayeyarwady (Irrawaddy) and Thanlwin (Salween) Rivers of Myanmar. *Quaternary International*, *186*(1), 113–122. Retrieved from

http://linkinghub.elsevier.com/retrieve/pii/S1040618207002170 doi: 10.1016/j.quaint.2007.08.003

Bouchez, J., Gaillardet, J., France-Lanord, C., Maurice, L., & Dutra-Maia, P. (2011, 3). Grain size control of river suspended sediment geochemistry: Clues from Amazon River depth profiles. *Geochemistry, Geophysics, Geosystems*, *12*(3), n/a-n/a. Retrieved from http://doi.wiley.com/10.1029/2010GC003380 doi: 10.1029/2010GC003380

Bouchez, J., Lupker, M., Gaillardet, J., France-Lanord, C., & Maurice, L. (2011, 11). How important is it to integrate riverine suspended sediment chemical composition with depth? Clues from Amazon River depth-profiles. *Geochimica et Cosmochimica Acta*, *75*(22), 6955–6970. Retrieved from https://linkinghub.elsevier.com/retrieve/pii/S0016703711005047 doi: 10.1016/j.gca.2011.08.038

Bouchez, J., Métivier, F., Lupker, M., Maurice, L., Perez, M., Gaillardet, J., & France-Lanord, C. (2011). Prediction of depth-integrated fluxes of suspended sediment in the Amazon River: Particle aggregation as a complicating factor. *Hydrological Processes*, *25*(5), 778–794. doi: 10.1002/hyp.7868

Chapman, H., Bickle, M., Thaw, S. H., & Thiam, H. N. (2015). Chemical fluxes from time series sampling of the Irrawaddy and Salween Rivers, Myanmar. *Chemical Geology*, *401*, 15–27. Retrieved from http://dx.doi.org/10.1016/j.chemgeo.2015.02.012 doi: 10.1016/j.chemgeo.2015.02.012

Chen, C. J., Senarath, S. U., Dima-West, I. M., & Marcella, M. P. (2017). Evaluation and restructuring of gridded precipitation data over the Greater Mekong Subregion. *International Journal of Climatology*, *37*(1), 180–196. doi: 10.1002/joc.4696

Darby, S. E., Hackney, C. R., Leyland, J., Kummu, M., Lauri, H., Parsons, D. R., ... Aalto, R. (2016). Fluvial sediment supply to a mega-delta reduced by shifting tropical-cyclone activity. *Nature*, *539*(7628), 276–279. Retrieved from http://dx.doi.org/10.1038/nature19809 doi: 10.1038/nature19809

D'Errico, J. (2018). *inpaint_nans*. MATLAB Central File Exchange. Retrieved from https://www.mathworks.com/matlabcentral/fileexchange/4551-inpaint_nans

Dietrich, W. E. (1982). Settling velocity of natural particles. *Water Resources Research*, *18*(6), 1615–1626. doi: 10.1029/WR018i006p01615

Diplas, P., Dancey, C. L., Celik, A. O., Valyrakis, M., Greer, K., & Akar, T. (2008, 10). The Role of Impulse on the Initiation of Particle Movement Under Turbulent Flow Conditions. *Science*, *322*(5902), 717–720. Retrieved from http://www.sciencemag.org/cgi/doi/10.1126/science.1158954 doi: 10.1126/science.1158954

France-Lanord, C., & Derry, L. (1997). Organic carbon burial forcing of the carbon cycle from Himalayan erosion. *Nature*, *390*(November), 65–67. Retrieved from http://www.es.ucsc.edu/~rcoe/eart206/France-Lanord&Derry_Nature97.pdf

Furuichi, T., Win, Z., & Wasson, R. J. (2009, 5). Discharge and suspended sediment transport in the Ayeyarwady River, Myanmar: centennial and decadal changes. *Hydrological Processes*, *23*(11), 1631–1641. Retrieved from http://doi.wiley.com/10.1002/hyp.7295 doi: 10.1002/hyp.7295

Gaillardet, J., Dupré, B., Louvat, P., & Allègre, C. (1999, 7). Global silicate weathering and CO2 consumption rates deduced from the chemistry of large rivers. *Chemical Geology*, *159*(1-4), 3–30. Retrieved from http://linkinghub.elsevier.com/retrieve/pii/S0009254199000315 doi: 10.1016/S0009-2541(99)00031-5

Galy, V., France-Lanord, C., Beyssac, O., Faure, P., Kudrass, H., & Palhol, F. (2007, 11). Efficient organic carbon burial in the Bengal fan sustained by the Himalayan erosional system. *Nature*, *450*(7168), 407–10. Re-

trieved from http://www.ncbi.nlm.nih.gov/pubmed/18004382 doi: 10.1038/nature06273

Galy, V., Peucker-Ehrenbrink, B., & Eglinton, T. (2015). Global carbon export from the terrestrial biosphere controlled by erosion. *Nature*, *521*(7551), 204–207. Retrieved from http://www.nature.com/doifinder/10.1038/nature14400 doi: 10.1038/nature14400

Godderis, Y., Roelandt, C., Schott, J., Pierret, M.-C., & Francois, L. M. (2009, 9). Towards an Integrated Model of Weathering, Climate, and Biospheric Processes. *Reviews in Mineralogy and Geochemistry*, *70*(1), 411–434. Retrieved from http://rimg.geoscienceworld.org/cgi/doi/10.2138/rmg.2009.70.9 doi: 10.2138/rmg.2009.70.9

Gordon, R. (1880). *Report on the Irawadi River. Pt I-IV.* (Tech. Rep.). Rangoon: Secretatriat.

Gray, J. R., & Gartner, J. W. (2009, 4). Technological advances in suspended-sediment surrogate monitoring. *Water Resources Research*, *45*(4). Retrieved from http://doi.wiley.com/10.1029/2008WR007063 doi: 10.1029/2008WR007063

Grill, G., Lehner, B., Thieme, M., Geenen, B., Tickner, D., Antonelli, F., ... Zarfl, C. (2019, 5). Mapping the world's free-flowing rivers. *Nature*, *569*(7755), 215–221. Retrieved from http://www.nature.com/articles/s41586-019-1111-9 doi: 10.1038/s41586-019-1111-9

Guo, L., & He, Q. (2011). Freshwater flocculation of suspended sediments in the Yangtze River, China. *Ocean Dynamics*, *61*(2-3), 371–386. doi: 10.1007/s10236-011-0391-x

Hackney, C. R., Darby, S. E., Parsons, D. R., Leyland, J., Best, J. L., Aalto, R., ... Houseago, R. C. (2020, 1). River bank instability from unsustainable sand mining in the lower Mekong River. *Nature Sustainability*. Retrieved from http://dx.doi.org/10.1038/s41893-019-0455-3http://www.nature.com/articles/s41893-019-0455-3 doi: 10.1038/s41893-019-0455-3

Hilton, R. G., Galy, A., Hovius, N., Chen, M.-C., Horng, M.-J., & Chen, H. (2008). Tropical-cyclone-driven erosion of the terrestrial biosphere from mountains. *Nature Geoscience*, *1*, 759–762. doi: 10.1038/ngeo333

Hilton, R. G., Galy, V., Gaillardet, J., Dellinger, M., Bryant, C., O'Regan, M., ... Calmels, D. (2015). Erosion of organic carbon in the Arctic as a geological carbon dioxide sink. *Nature*, *524*(7563), 84–87. doi: 10.1038/nature14653

Horan, K., Hilton, R., Dellinger, M., Tipper, E., Galy, V., Calmels, D., ... Burton, K. (2019). Carbon dioxide emissions by rock organic carbon oxidation and the net geochemical carbon budget of the Mackenzie River Basin. *American Journal of Science*, *319*, 473–499. doi: 10.2475/06.2019.02

Jordan, P. (1965). *Fluvial sediment of the mississippi river at St. Louis, Missouri* (Tech. Rep.). United States Army. Corps of Engineers. Retrieved from http://pubs.usgs.gov/wsp/1802/report.pdf

Khin Zaw, Win Swe, Barber, A. J., Crow, M. J., & Yin Yin Nwe. (2017, 11). Introduction to the geology of Myanmar. *Geological Society, London, Memoirs*, *48*(1), 1–17. Retrieved from http://mem.lyellcollection.org/lookup/doi/10.1144/M45.01http://mem.lyellcollection.org/lookup/doi/10.1144/M48.1 doi: 10.1144/M48.1

Kirchherr, J., J. Charles, K., & Walton, M. J. (2017). The interplay of activists and dam developers: the case of Myanmar's mega-dams. *International Journal of Water Resources Development*, *33*(1), 111–131. Retrieved from http://dx.doi.org/10.1080/07900627.2016.1179176 doi: 10.1080/07900627.2016.1179176

Komada, T., Anderson, M. R., & Dorfmeier, C. L. (2008). Carbonate removal from coastal sediments for the determination of organic carbon and its isotopic signatures, δ 13 C and Δ 14 C: comparison of fumigation and direct acidification

by hydrochloric acid. *Limnology and Oceanography: Methods*, *6*(6), 254–262. doi: 10.4319/lom.2008.6.254

Kondolf, G. M., Schmitt, R. J., Carling, P., Darby, S., Arias, M., Bizzi, S., ... Wild, T. (2018). Changing sediment budget of the Mekong: Cumulative threats and management strategies for a large river basin. *Science of the Total Environment*, *625*, 114–134. Retrieved from `https://doi.org/10.1016/j.scitotenv.2017.11.361` doi: 10.1016/j.scitotenv.2017.11.361

Kostaschuk, R., Best, J., Villard, P., Peakall, J., & Franklin, M. (2005). Measuring flow velocity and sediment transport with an acoustic Doppler current profiler. *Geomorphology*, *68*(1-2), 25–37. doi: 10.1016/j.geomorph.2004.07.012

Latosinski, F. G., Szupiany, R. N., García, C. M., Guerrero, M., & Amsler, M. L. (2014). Estimation of Concentration and Load of Suspended Bed Sediment in a Large River by Means of Acoustic Doppler Technology. *Journal of Hydraulic Engineering*, *140*(7), 04014023. Retrieved from `http://ascelibrary.org/doi/10.1061/%28ASCE%29HY.1943-7900.0000859` doi: 10.1061/(ASCE)HY.1943-7900.0000859

Lazarus, K., Cardinale, P., Corbett, M., Lin, N. S., & Noeske, T. (2019). *Strategic Environmental Assessment of the Hydropower Sector in Myanmar : Baseline Assessment Report* (Tech. Rep.). Washington, D.C: World Bank Group. Retrieved from `http://documents.worldbank.org/curated/en/126001548867293771/Baseline-Assessment-Report-Introduction`

Licht, A., France-Lanord, C., Reisberg, L., Fontaine, C., Soe, A. N., & Jaeger, J.-J. (2013). A palaeo Tibet–Myanmar connection? Reconstructing the Late Eocene drainage system of central Myanmar using a multi-proxy approach. *Journal of the Geological Society*, *170*(6), 929–939. Retrieved from `http://jgs.lyellcollection.org/lookup/doi/10.1144/jgs2012-126` doi: 10.1144/jgs2012-126

Lupker, M., France-Lanord, C., Lavé, J., Bouchez, J., Galy, V., Métivier, F., ... Mugnier, J.-L. (2011, 11). A Rouse-based method to integrate the chemical composition of river sediments: Application to the Ganga basin. *Journal of Geophysical Research*, *116*(F4), F04012. Retrieved from `http://doi.wiley.com/10.1029/2010JF001947` doi: 10.1029/2010JF001947

Mackenzie, F. T., & Garrels, R. M. (1966, 9). Chemical mass balance between rivers and oceans. *American Journal of Science*, *264*(7), 507–525. Retrieved from `http://www.ajsonline.org/cgi/doi/10.2475/ajs.264.7.507` doi: 10.2475/ajs.264.7.507

Maher, K., & Chamberlain, C. P. (2014, 3). Hydrologic regulation of chemical weathering and the geologic carbon cycle. *Science*, *343*(6178), 1502–4. Retrieved from `http://science.sciencemag.org/content/343/6178/1502.long` doi: 10.1126/science.1250770

Meade, R. H. (1994). Suspended sediments of the modern Amazon and Orinoco rivers. *Quaternary International*, *21*(C), 29–39. doi: 10.1016/1040-6182(94)90019-1

Meade, R. H., & Stevens, H. H. (1990). Strategies and equipment for sampling suspended sediment and associated toxic chemicals in large rivers - With emphasis on the Mississippi river. *Science of the Total Environment, The*, *97-98*(C), 125–135. doi: 10.1016/0048-9697(90)90235-M

Meybeck, M. (1987). *Global Chemical Weathering of Surficial Rocks Estimated From River Dissolved Loads.* (Vol. 287) (No. 5). doi: 10.2475/ajs.287.5.401

Meybeck, M., & Ragu, A. (1997). *River discharges to the oceans: an assessment of suspended solids, major ions and nutrients* (Tech. Rep.). UNEP.

Miller, M., McCave, I. N., & Komar, P. (1977). Threshold of sediment motion under unidirectional currents. *Sedimentology*, 507–527. doi: 10.1111/j.1365-3091.1977.tb00136.x

Milliman, J. D., & Farnsworth, K. L. (2011). *River Discharge to the Coastal*

Ocean. Cambridge: Cambridge University Press. Retrieved from http://ebooks.cambridge.org/ref/id/CBO9780511781247 doi: 10.1017/CBO9780511781247

Mitchell, A., Chung, S. L., Oo, T., Lin, T. H., & Hung, C. H. (2012). Zircon U-Pb ages in Myanmar: Magmatic-metamorphic events and the closure of a neo-Tethys ocean? *Journal of Asian Earth Sciences*, *56*, 1–23. Retrieved from http://dx.doi.org/10.1016/j.jseaes.2012.04.019 doi: 10.1016/j.jseaes.2012.04.019

Morin, G. P., Lavé, J., France-Lanord, C., Rigaudier, T., Gajurel, A. P., & Sinha, R. (2018). Annual Sediment Transport Dynamics in the Narayani Basin, Central Nepal: Assessing the Impacts of Erosion Processes in the Annual Sediment Budget. *Journal of Geophysical Research: Earth Surface*, *123*(10), 2341–2376. doi: 10.1029/2017JF004460

Murray Hicks, D., & Gomez, B. (2016, 4). Sediment transport. In G. Kondolf & H. Piégay (Eds.), *Tools in fluvial geomorphology* (2nd ed., pp. 324–356). Chichester, UK: Wiley. Retrieved from https://doi.org/10.1002/9781118648551.ch15https://onlinelibrary.wiley.com/doi/abs/10.1002/9781118648551.ch15 doi: 10.1002/9781118648551.ch15

Muste, M., Yu, K., Fujita, I., & Ettema, R. (2005). Two-phase versus mixed-flow perspective on suspended sediment transport in turbulent channel flows. *Water Resources Research*, *41*(10). doi: 10.1029/2004WR003595

Najman, Y., Sobel, E. R., Millar, I., Stockli, D. F., Govin, G., Lisker, F., ... Kahn, A. (2020, 1). The exhumation of the Indo-Burman Ranges, Myanmar. *Earth and Planetary Science Letters*, *530*, 115948. Retrieved from https://linkinghub.elsevier.com/retrieve/pii/S0012821X19306405 doi: 10.1016/j.epsl.2019.115948

Pal, D., & Ghoshal, K. (2016). Effect of particle concentration on sediment and turbulent diffusion coefficients in open-channel turbulent flow. *Environmental Earth Sciences*, *75*(18), 1–11. doi: 10.1007/s12665-016-6045-z

Parsons, D. R., Jackson, P. R., Czuba, J. A., Engel, F. L., Rhoads, B. L., Oberg, K. A., ... Riley, J. D. (2013). Velocity Mapping Toolbox (VMT): A processing and visualization suite for moving-vessel ADCP measurements. *Earth Surface Processes and Landforms*, *38*(11), 1244–1260. doi: 10.1002/esp.3367

Robinson, R., Bird, M., Oo, N. W., Hoey, T., Aye, M. M., Higgitt, D., ... Win, S. L. (2007, 11). The Irrawaddy River Sediment Flux to the Indian Ocean: The Original Nineteenth-Century Data Revisited. *The Journal of Geology*, *115*(6), 629–640. Retrieved from https://www.jstor.org/stable/10.1086/521607https://www.journals.uchicago.edu/doi/10.1086/521607 doi: 10.1086/521607

Rouse, H. (1950). Fundamental principles of flow. *Engineering hydraulics*, 1–135.

Santini, W., Camenen, B., Le Coz, J., Vauchel, P., Guyot, J.-L., Lavado, W., ... Martinez, J.-M. (2019). An index concentration method for suspended load monitoring in large rivers of the Amazonian foreland. *Earth Surface Dynamics*, 1–36. doi: 10.5194/esurf-2018-93

Searle, M. P., Noble, S. R., Cottle, J. M., Waters, D. J., Mitchell, A. H., Hlaing, T., & Horstwood, M. S. (2007). Tectonic evolution of the Mogok metamorphic belt, Burma (Myanmar) constrained by U-Th-Pb dating of metamorphic and magmatic rocks. *Tectonics*, *26*(3). doi: 10.1029/2006TC002083

Sein, K. K., Chidthaisong, A., & Oo, K. L. (2018). Observed Trends and Changes in Temperature and Precipitation Extreme Indices over Myanmar. *Atmosphere*, *9*(12), 477. Retrieved from https://doi.org/10.3390/atmos9120477 doi: 10.3390/atmos9120477

Syvitski, J. P., & Kettner, A. (2011). Sediment flux and the anthropocene. *Philosophical Transactions of the Royal Society A: Mathematical, Physical and Engineering Sciences*, *369*(1938), 957–975. doi: 10.1098/rsta.2010.0329

Syvitski, J. P., Vörösmarty, C. J., Kettner, A. J., & Green, P. (2005). Impact of humans on the flux of terrestrial sediment to the global coastal ocean. *Science*, *308*(5720), 376–380. doi: 10.1126/science.1109454

Szupiany, R. N., Amsler, M. L., Best, J. L., & Parsons, D. R. (2007). Comparison of Fixed- and Moving-Vessel Flow Measurements with an aDp in a Large River. *Journal of Hydraulic Engineering*, *133*(12), 1299–1309. doi: 10.1061/(asce)0733-9429(2007)133:12(1299)

Szupiany, R. N., Lopez Weibel, C., Guerrero, M., Latosinski, F., Wood, M., Dominguez Ruben, L., & Oberg, K. (2019, 5). Estimating sand concentrations using ADCP-based acoustic inversion in a large fluvial system characterized by bi-modal suspended-sediment distributions. *Earth Surface Processes and Landforms*, *44*(6), 1295–1308. Retrieved from `https://onlinelibrary.wiley.com/doi/abs/10.1002/esp.4572` doi: 10.1002/esp.4572

Thorne, P. D., & Hanes, D. M. (2002, 3). A review of acoustic measurement of small-scale sediment processes. *Continental Shelf Research*, *22*(4), 603–632. Retrieved from `https://linkinghub.elsevier.com/retrieve/pii/S0278434301001017` doi: 10.1016/S0278-4343(01)00101-7

van Rijn, L. C., Walstra, D.-J. R., & van Ormondt, M. (2007). Unified View of Sediment Transport by Currents and Waves. IV: Application of Morphodynamic Model. *Journal of Hydraulic Engineering*, *133*(7), 776–793. Retrieved from `http://ascelibrary.org/doi/10.1061/%28ASCE%290733-9429%282007%29133%3A7%28776%29` doi: 10.1061/(ASCE)0733-9429(2007)133:7(776)

Viers, J., Oliva, P., Dandurand, J. L., Dupr??, B., & Gaillardet, J. (2013). Chemical Weathering Rates, CO2 Consumption, and Control Parameters Deduced from the Chemical Composition of Rivers. In *Treatise on geochemistry: Second edition* (Vol. 7, pp. 175–194). doi: 10.1016/B978-0-08-095975-7.00506-4

Wang, H., Yang, Z., Saito, Y., Liu, J. P., Sun, X., & Wang, Y. (2007). Stepwise decreases of the Huanghe (Yellow River) sediment load (1950-2005): Impacts of climate change and human activities. *Global and Planetary Change*, *57*(3-4), 331–354. doi: 10.1016/j.gloplacha.2007.01.003

West, A., Galy, A., & Bickle, M. (2005, 6). Tectonic and climatic controls on silicate weathering. *Earth and Planetary Science Letters*, *235*(1-2), 211–228. Retrieved from `http://linkinghub.elsevier.com/retrieve/pii/S0012821X05002116` doi: 10.1016/j.epsl.2005.03.020

Westerweel, J., Roperch, P., Licht, A., Dupont-Nivet, G., Win, Z., Poblete, F., ... Aung, D. W. (2019). Burma Terrane part of the Trans-Tethyan arc during collision with India according to palaeomagnetic data. *Nature Geoscience*, *12*(October). Retrieved from `http://dx.doi.org/10.1038/s41561-019-0443-2` doi: 10.1038/s41561-019-0443-2

Wilkinson, B. H., & McElroy, B. J. (2007). The impact of humans on continental erosion and sedimentation. *Bulletin of the Geological Society of America*, *119*(1-2), 140–156. doi: 10.1130/B25899.1

Xiqing, C., Qiaoju, Z., & Erfeng, Z. (2006). In-channel sand extraction from the mid-lower Yangtze channels and its management: Problems and challenges. *Journal of Environmental Planning and Management*, *49*(2), 309–320. doi: 10.1080/09640560500508247

Yamazaki, D., Ikeshima, D., Sosa, J., Bates, P. D., Allen, G., & Pavelsky, T. (2019). MERIT Hydro: A high-resolution global hydrography map based on latest topography datasets. *Water Resources Research*, 2019WR024873. Retrieved from `https://onlinelibrary.wiley.com/doi/abs/10.1029/2019WR024873` doi: 10.1029/2019WR024873

Yorke, T. H., & Oberg, K. A. (2002). Measuring river velocity and discharge with acoustic Doppler profilers. *Flow Measurement and Instrumentation*, *13*(5-6), 191–195. doi: 10.1016/S0955-5986(02)00051-1

Zhang, J., Xiao, W., Windley, B. F., Wakabayashi, J., Cai, F., Sein, K., ... Naing, S. (2018). *Multiple alternating forearc- and backarc-ward migration of magmatism in the Indo-Myanmar Orogenic Belt since the Jurassic: Documentation of the orogenic architecture of eastern Neotethys in SE Asia* (Vol. 185) (No. January). Elsevier. Retrieved from `https://doi.org/10.1016/j.earscirev.2018.07.009` doi: 10.1016/j.earscirev.2018.07.009

Supporting Information for "Integrating suspended sediment flux in large, morphologically complex river channels: Application of a synoptic Rouse-based model to the Irrawaddy and Salween rivers"

J. Jotautas Baronas[1], Emily I. Stevenson[1], Christopher R. Hackney[2,3], Stephen E. Darby[4], Michael J. Bickle[1], Robert G. Hilton[5], Christina S. Larkin[1], Daniel R. Parsons[2], Aung Myo Khaing[6], Edward T. Tipper[1]

[1]Dept. of Earth Sciences, University of Cambridge, UK

[2]Energy and Environmental Institute, University of Hull, UK

[3]School of Geography, Politics and Sociology, Newcastle University, UK

[4]School of Geography and Environmental Science, University of Southampton, UK

[5]Dept. of Geography, Durham University, UK

[6]Directorate of Water Resources and Improvement of River Systems, Yangon, Myanmar

Contents of this file

Additional Supporting Information (Files uploaded separately)

Captions for large Tables S1 and S4:

Table S1. Measured and model-recalculated sample compositions.

Table S4. Mean monthly sediment concentration and composition calculated using the rating curves given in Table S3, as well as the water discharge values used.

Text S1. Hydrodynamic sediment transport model details

Calculating shear velocity

To calculate the sediment flux variations laterally across the width of the river channel, it is necessary to establish a relationship between C_i and the prevailing hydrodynamic conditions, which can be represented by boundary shear stress or shear velocity. There are several methods available to determine the boundary shear stress τ_0, which can be easily converted to shear velocity ($u^* = \sqrt{\tau_0/\rho}$, where ρ is fluid density). The different methods, their (dis)advantages, and the data required by each have been summarized by Dietrich and Whiting (1989). In our case, the most reliable and practical approach is to use the velocity measurements obtained by ADCP, employing the approach first tested by Wilcock (1996):

$$u^* = \frac{u \ \cdot \kappa}{ln(\frac{z}{d})} \tag{S1}$$

where $\kappa = 0.41$ is the von Karman constant and $d = 0.1 \cdot D_{84}^{bedload}$ is an estimate of bed roughness. This approach ignores other potential sources of drag, such as bedform, bank, and wind resistance, that may influence the velocity profile (Dietrich & Whiting, 1989). For this reason, u^* has been typically estimated using velocity measurements in the near-bed region that is both high above the bed to avoid bedform drag and low enough below the free surface, where secondary flow effects can influence the velocity structure

(e.g., $3D_{84} < z < 0.2H$) (Wilcock, 1996). More recently, Sime, Ferguson, and Church (2007) have shown that in the case of the Fraser river, velocity profiles integrated over the full depth (H) gave the most accurate estimates of u^*, in which case Eq. S1 becomes:

$$u^* = \frac{\overline{u} \cdot \kappa}{ln(\frac{H}{e \cdot d})} \tag{S2}$$

where $\overline{u}$ is the depth-averaged velocity and e is the base of the natural logarithm. Eq. S2 has been later shown to also work well for the Ganges river by Lupker et al. (2011). This is the approach we have adopted in this study, too.

To enable a fit of the Rouse model, shear velocity needs to be calculated for each collected sediment sample. In August 2017, ADCP data were collected only during discharge transects but not simultaneously while collecting depth samples, and therefore relevant velocity data was extracted from a subsection of MCS closest to the sediment sample collected on the same day. For all other samples, $\overline{u}$ was extracted from ADCP data recorded during sample collection, using a time-averaged velocity profile. However, it is difficult to know which timescale is the most relevant for sediment suspension and therefore should be used in the model. We typically collected 3-10 min of water velocity data while drifting with river flow to collect isokinetic sediment samples (examples in Figs S1-S2). We have tested two different timescales for time-averaging velocity data: 1) 10 sec prior to sample collection (reflecting "instantaneous" hydrodynamic conditions) and 2) 2 min before and 2 min after sample collection (4 min total, reflecting time-integrated "steady-state" hydrodynamic conditions). There was no simple relationship between either of the u^* values and sampled sediment concentrations. For example, "outlier" samples with high SSC at mid- or low-depths often did not coincide with higher u^* values, regardless of the timescale

used. As a result, the choice of one u^* value over the other (10-sec vs 4-min integration time) made a relatively small difference to the final model results. Because the measured SSC values vary over a larger relative range, they influence the regression fit more strongly than the selection of u^*. Ultimately, we chose to use the 10-sec integrated u^* values, as in some cases the hydrodynamic conditions were observed to shift significantly during the 4 minute drift window, e.g., due to shoaling of the river channel (Fig. S2), or drift towards the river bank, such that the 4-minute integrated u^* value is unlikely to be reflective of the hydrodynamic conditions during the time of sample collection.

Empirically fitting the Rouse equation

Having obtained a shear velocity value for each depth sample as described above, a least-squares regression of Eq. 4 can be performed to obtain fitted parameters C_0^i and b_i for each grainsize bin i (summarized in Table S2). This was done using a non-linear fit regression function in MATLAB 2019b (*fitnlm*, Statistics and Machine Learning Toolbox), using a constant-error χ^2 minimization. The initial parameters were supplied as $C_0^i = \overline{C}_i^{meas}$ and $b_i = 0$, where $\overline{C}_i^{meas}$ is the mean of all measured sediment concentrations in grainsize bin i at a given site, given in Supp. Table S1. It is important that the regression is done in power law form, rather a log-log transform of Eq. 4 as this introduces a very large error at high u^* values. The full non-linear model fits, as well as their covariance matrices, fitted data residuals, and various goodness-of-fit statistics are given in the Supplementary Material as MATLAB model objects.

Applying Rouse model fit to channel cross-sections

The Rouse model fits determined above were applied to ADCP flow velocity cross-sections (such as shown in Fig. 2) to synoptically predict sediment distribution and composition in both dimensions across the MCS. For each pre-processed velocity MCS (see Methods), the depth-averaged shear velocity was calculated laterally across the channel using Eq. S2. Eq. 4 was then used to calculate sediment concentrations binned by grainsize (C_i) using the five sets of fitted parameters (Supp. Table S2).

To obtain an uncertainty estimate of the model results we used the MATLAB 2019b *predict* function, which employs the non-linear model equations constructed by the *fitnlm* function (Supp. Table S2) to calculate predicted C_i values over the distribution of measured u^* and Rouse depth values (calculated for each ADCP cross section as described above), along with confidence bounds that take into account model parameter covariance. As implemented in MATLAB 2019b, the confidence bounds are calculated using a hybrid Scheffé-Bonferroni approach, described in Lane and Dumouchel (1994). We set the *predict* function to calculate 68% confidence bounds for all predicted C_i values in a given cross-section simultaneously (i.e. bounding the mean sediment concentration ($\overline{C}_i^{MCS}$) calculated over the whole cross-section). As a result, the uncertainty of C_i^{MCS} values calculated for each *individual* ADCP data bin may be underestimated; however, we are more interested in the uncertainty of $\overline{C}_i^{MCS}$, i.e. the mean sediment concentration integrated over the *whole* cross-section. The lower and upper bounds of each of the five $\overline{C}_i^{MCS}$ values were summed to obtain the total mean SSC uncertainty, while the sediment flux Q_S confidence bounds (as reported in Table 1) were obtained by applying Eqs. 5 and 6 to the lower and upper bounds of all C_i^{MCS} values simultaneously.

Text S2. Calculating bedload flux

The laterally-resolved bedload flux $[kg\ m^{-1}\ s^{-1}]$ was calculated using the semi-empirical calibration of van Rijn, Walstra, and van Ormondt (2007), previously applied by Lupker et al. (2011) to the Ganges River:

$$q_b(x) = 0.015 \cdot \rho_s \cdot \overline{u}(x) \cdot H(x) \cdot \Big(\frac{D_{50}^{bed}}{H}\Big)^{1.2} \cdot (M_e)^{1.5};\ M_e = \frac{\overline{u}(x) - \overline{u}_{cr}}{\sqrt{R \cdot g \cdot D_{50}^{bed}}} \qquad \text{(S3)}$$

where ρ_s is the sediment specific gravity ($= 2.65\ g\ cm^{-3}$), $R = (\rho_s - \rho_w)/\rho_w$, g the gravitational constant, and $\overline{u}_{cr}$ the depth-averaged critical velocity for the initiation of motion for bedload particles of size equal to D_{50}^{bed} (615 and 506 μm for Irrawaddy and Salween, respectively, measured on dredged bedload samples), calculated using Eq. S1 and the D_{50}-u^* relationship given in Fig. 3 of Miller, McCave, and Komar (1977), indicating values of 0.019 and 0.018 m/s for Irrawaddy and Salween bedloads, respectively. In parts of the river channel where $\overline{u}(x) < \overline{u}_{cr}$, q_b was set equal to 0. The total bedload flux across the river channel $[kg\ s^{-1}]$ is then obtained by lateral integration across the channel:

$$Q_b = \int q_b(x) \cdot dx \qquad \text{(S4)}$$

The Q_b value calculated for each cross-section was added to the suspended sediment flux Q_s calculated using the semi-empirical Rouse model described above (Eq. 6) and the total sediment flux reported in Table 1 is the sum of both values. Because in all cases $Q_b < 3\%$ of Q_s, the uncertainty of the bedload flux and its contribution to the POC flux were neglected in further calculations.

Text S3. Temporal integration of sediment flux and composition details

Estimating monthly Salween discharge

In the absence of monthly Salween discharge measurements, we used our ADCP data determined on four dates (simultaneously within a span of 2 days at each site; Table 1) to estimate the monthly Salween discharge at Hpa-An. To do this, we calculated the average Irrawaddy / Salween discharge ratio for each season (averaging two values for each season), obtaining ratios of 0.36 for August and 0.55 for February/May. The ratios for other months were interpolated to vary between these two values. In August 2017, the Irrawaddy discharge was very high (ratio of 0.28) and in August 2018 the Salween water was at a 100-year flood level according to locals (ratio of 0.45). The two years therefore probably represent close to extremes of possible ratios and, in the absence of any other data, we speculate that the average value of 0.36 may be reasonably representative of typical Irrawaddy/Salween discharge ratio in August. The dry season discharge ratio is much less critical due to the highly monsoonal character of both rivers.

Using this approach, our calculated monthly Salween discharge for May-Oct is slightly lower than that measured in 2004 (Chapman et al., 2015), with a maximum of 10,700 m^3/s in August. Given that our measured instantaneous discharge of 14,300 m^3/s represented a 100-year flood, we deem this monthly average of 10,700 m^3/s more likely close to long-term average than the 12,700 and 13,100 m^3/s measured in August and September 2004 respectively (Chapman et al., 2015), which was a relatively wet year (Sein et al., 2015).

Suspended sediment - discharge rating curves

Sediment-discharge rating curves were calculated separately for each SSC grainsize bin i (Fig. 9), linearly regressing mean C_i vs. Q_w in log-log space:

$$log_{10}(C_i) = m_i \cdot log_{10}(Q_w) + n_i \tag{S5}$$

where m_i and n_i are fitted parameters. The mean C_i values were calculated for each sampling date (n = 4) on each river (Table 1), using the hydrodynamic modeling approach described in Section 3 and Supp. Text S1. The degrees-of-freedom adjusted R^2 values ranged between 0.94 and 0.99, reflecting the close correlation between C_i and Q_w. All rating curve parameters and goodness-of-fit statistics are given in the Supplementary Table S3. The minimum, best, and maximum estimates of $C_1 - C_5$ (Supp .Table S4) were calculated using the 68% confidence interval of the C_i vs. Q_w rating curves (Supp. Table S3), using MATLAB 2019b function *predint* that takes into account the covariance of regression fit parameters.

Although each rating curve has only four data points, they cover the two extremes of discharge in each river, comfortably bracketing monthly mean values (Fig. 7a). It might be argued that the lack of intermediate data does not allow us to constrain the functional form of the rating curves, however, the slope of a log-log linear regression (i.e. log-transformed power law) such as that used here is most strongly constrained by values at the two extreme ends of the relationship. A linear regressionin log-log space has been established as the most robust functional form for SSC and POC rating curves in many rivers globally (Ferguson, 1986; Crawford, 1991; Syvitski et al., 2000; Warrick, 2015; Clark et al., 2017). However, it has been shown that transformation back from log-log space can result in a systematic error of the predicted SSC values due to the fact that a log-log linear regression minimizes the residuals around geometric mean, rather than arithmetic mean, resulting in a bias when log-log fitted values are converted back to linear space (Ferguson,

1986). Using the proposed approach of Ferguson (1986), which corrects for this bias and which has been employed by many researchers since, we calculated and applied correction factors to the monthly (and annual) predicted SSC concentrations, thus also correcting the calculated sediment fluxes. The correction factors ranged from 1.006 to 1.104 (i.e. bias ranging between 0.6 and 10.4%) and were highest for the coarsest grainsize bin (i = 5), which is the most sensitive to discharge (Supp. Table S3).

Monthly and annual means of sediment composition and flux

The monthly grain size parameters (D_{50} and D_{84}) were calculated from the suspended sediment concentrations in the five size fractions ($C_1 - C_5$) each month (Supp. Table S4). To do this, the 5-bin cumulative grain size distribution was interpolated using shape-preserving piecewise cubic interpolation algorithm (*pchip* function in MATLAB 2019b) and resampled at 10,000 logarithmically-spaced bins, then finding the bin closest to the 50th and 84th percentile for D_{50} and D_{84} , respectively. This procedure was applied to the minimum, best, and maximum estimates of $C_1 - C_5$ to calculate uncertainty in D_{50} and D_{84}.

The monthly %OC values were then calculated using the %OC vs D_{50} correlation determined from sediment analyses (Fig. 6). The lower bound of monthly %OC uncertainty is reported as the lower confidence interval bound (16th percentile) of the %OC vs D_{50} fit, applied to the minimum D_{50} estimate each month (Supp. Table S4). Equivalently, the upper bound of uncertainty is reported as the upper confidence interval bound (84th percentile) of the %OC vs D_{50} fit (Fig. 6), applied to the upper maximum monthly estimates of D_{50}. POC concentrations in mg/L were then calculated as the product of %OC and SSC (Supp. Table S4).

Monthly fluxes were calculated by multiplying the monthly discharge with monthly SSC and POC values (Supp. Table S4). For the Irrawaddy, this represents the monthly averages over 31 years, whereas for Salween the monthly values are already estimated as a long-term average (see above). All annual values were calculated as flux-weighted average of the monthly values. The monthly and the summed annual values therefore represent a 1 σ, fully propagated uncertainty. Because the fraction of bedload flux did not vary strongly with discharge, the total monthly and annual sediment flux was calculated by adding the mean bedload flux fraction (calculated across the four dates at each site) to the suspended sediment flux:

$$Q_{s+b} = Q_s \cdot \left(1 + (\frac{\overline{Q_b}}{Q_s})\right) \tag{S6}$$

Because bedload flux represented a small fraction ($< 3\%$) of total sediment flux in all cases, uncertainty in bedload flux was disregarded for simplicity.

References

Chapman, H., Bickle, M., Thaw, S. H., & Thiam, H. N. (2015). Chemical fluxes from time series sampling of the Irrawaddy and Salween Rivers, Myanmar. *Chemical Geology*, *401*, 15–27. Retrieved from `http://dx.doi.org/10.1016/j.chemgeo.2015.02.012` doi: 10.1016/j.chemgeo.2015.02.012

Clark, K. E., Hilton, R. G., West, A. J., Robles Caceres, A., Gröcke, D. R., Marthews, T. R., ... Malhi, Y. (2017). Erosion of organic carbon from the Andes and its effects on ecosystem carbon dioxide balance. *Journal of Geophysical Research: Biogeosciences*, 5825–5846. Retrieved from `http://doi.wiley.com/`

10.1002/2016JG003615 doi: 10.1002/2016JG003615

Crawford, C. G. (1991). Estimation of suspended-sediment rating curves and mean suspended-sediment loads. *Journal of Hydrology*, *129*(1-4), 331–348. doi: 10.1016/0022-1694(91)90057-O

Dietrich, W. E., & Whiting, P. (1989). Boundary shear stress and sediment transport in river meanders of sand and gravel. In *River meandering* (Vol. 12, pp. 1–50). Retrieved from http://www.agu.org/books/wm/v012/WM012p0001/WM012p0001.shtml doi: 10.1029/WM012p0001

Ferguson, R. I. (1986). River Loads Underestimated by Rating Curves. *Water Resources Research*, *22*(1), 74–76. doi: 10.1029/WR022i001p00074

Lane, T. P., & Dumouchel, W. H. (1994). Simultaneous confidence intervals in multiple regression. *American Statistician*, *48*(4), 315–321. doi: 10.1080/00031305.1994.10476090

Lupker, M., France-Lanord, C., Lavé, J., Bouchez, J., Galy, V., Métivier, F., ... Mugnier, J.-L. (2011, 11). A Rouse-based method to integrate the chemical composition of river sediments: Application to the Ganga basin. *Journal of Geophysical Research*, *116*(F4), F04012. Retrieved from http://doi.wiley.com/10.1029/2010JF001947 doi: 10.1029/2010JF001947

Miller, M., McCave, I. N., & Komar, P. (1977). Threshold of sediment motion under unidirectional currents. *Sedimentology*, 507–527. doi: 10.1111/j.1365-3091.1977.tb00136.x

Sein, M. M. Z., Ogwang, B. A., Ongoma, V., Ogou, F. K., & Batebana, K. (2015). Interannual variability of Summer Monsoon Rainfall over Myanmar in relation to IOD and

ENSO. *Journal of Environmental and Agricultural Sciences*, *4*(February 2018), 2313–8629. Retrieved from http://www.researchgate.net/publication/278465029

Sime, L. C., Ferguson, R. I., & Church, M. (2007). Estimating shear stress from moving boat acoustic Doppler velocity measurements in a large gravel bed river. *Water Resources Research*, *43*(3), 1–12. doi: 10.1029/2006WR005069

Syvitski, J. P., Morehead, M. D., Bahr, D. B., & Mulder, T. (2000). Estimating fluvial sediment transport: The rating parameters. *Water Resources Research*, *36*(9), 2747–2760. doi: 10.1029/2000WR900133

van Rijn, L. C., Walstra, D.-J. R., & van Ormondt, M. (2007). Unified View of Sediment Transport by Currents and Waves. IV: Application of Morphodynamic Model. *Journal of Hydraulic Engineering*, *133*(7), 776–793. Retrieved from http://ascelibrary.org/doi/10.1061/%28ASCE%290733-9429%282007%29133%3A7%28776%29 doi: 10.1061/(ASCE)0733-9429(2007)133:7(776)

Warrick, J. A. (2015). Trend analyses with river sediment rating curves. *Hydrological Processes*, *29*(6), 936–949. doi: 10.1002/hyp.10198

Wilcock, P. R. (1996). Estimating local bed shear stress from velocity observations. *Water Resources Research*, *32*(11), 3361–3366. doi: 10.1029/96WR02277

Table S2. Hydrodynamic Rouse model (Eq. 4) parameters obtained by non-linear least-squares regression of u^*, z_r, and C_i data given in Supp. Table S1. The three-dimensional fit surfaces shown in Fig. 3 were calculated using the Salween parameter values given here. The uncertainty of each fitted parameter is given as standard error (i.e., square root of variance). RMSE is root mean square error between the data and the fitted model. F-stat is the F-statistic of the overall model significance relative to null-hypothesis. All p-values are $<< 0.01$ (not shown).

Grainsize bin		Fitted parameters		Goodness-of-fit		
Irrawaddy (Pyay)		C_0^i	b_i	Adj. R^2	RMSE	F-stat
0.4-4 μm	i=1	0.417 ± 0.054	0.0073 ± 0.0013	0.65	0.0662	126
4-16 μm	i=2	0.529 ± 0.063	0.0064 ± 0.0011	0.63	0.0853	143
16-63 μm	i=3	0.95 ± 0.17	0.012 ± 0.002	0.61	0.131	75.6
63-250 μm	i=4	1.96 ± 0.55	0.017 ± 0.004	0.46	0.334	28.6
250-2500 μm	i=5	2.84 ± 0.8	0.029 ± 0.006	0.55	0.249	31.4
Salween (Hpa-An)						
0.4-4 μm	i=1	0.701 ± 0.146	0.0114 ± 0.0025	0.61	0.0887	88.4
4-16 μm	i=2	1.55 ± 0.33	0.0123 ± 0.0026	0.62	0.187	84.8
16-63 μm	i=3	2.3 ± 0.77	0.015 ± 0.004	0.47	0.339	36.1
63-250 μm	i=4	19.79 ± 6.81	0.046 ± 0.008	0.62	0.595	31.2
250-2500 μm	i=5	16.46 ± 6.19	0.06 ± 0.01	0.76	0.231	50.1

Table S3. Susp. sediment concentration (C_i) vs water discharge (Q_w) rating curve parameters (Eq. S5) and their 68% confidence intervals, goodness-of-fit statistics, and log-log bias correction factors (see Supp. Text S3).

Grainsize bin		**Fitted parameters**						**Goodness-of-fit**		
		slope			intercept			Adj. R^2	RMSE	Corr. factor
Irrawaddy (Pyay)		min	mean	max	min	mean	max			
0.4-4 μm	i=1	0.43	0.50	0.56	-3.26	-2.98	-2.70	0.97	0.05	1.007
4-16 μm	i=2	0.38	0.45	0.51	-2.86	-2.61	-2.35	0.97	0.05	1.006
16-63 μm	i=3	0.68	0.78	0.88	-4.53	-4.13	-3.73	0.97	0.07	1.014
63-250 μm	i=4	0.87	0.98	1.10	-5.38	-4.92	-4.46	0.98	0.08	1.019
250-2500 μm	i=5	1.33	1.46	1.58	-7.89	-7.36	-6.84	0.99	0.10	1.025
Salween (Hpa-An)		min	mean	max	min	mean	max			
0.4-4 μm	i=1	0.59	0.73	0.87	-4.14	-3.63	-3.12	0.94	0.08	1.018
4-16 μm	i=2	0.63	0.77	0.91	-4.02	-3.49	-2.95	0.94	0.09	1.020
16-63 μm	i=3	0.75	0.92	1.09	-4.67	-4.05	-3.42	0.94	0.10	1.027
63-250 μm	i=4	1.57	1.84	2.11	-8.93	-7.91	-6.88	0.96	0.16	1.074
250-2500 μm	i=5	1.81	2.13	2.45	-10.75	-9.56	-8.36	0.96	0.19	1.104

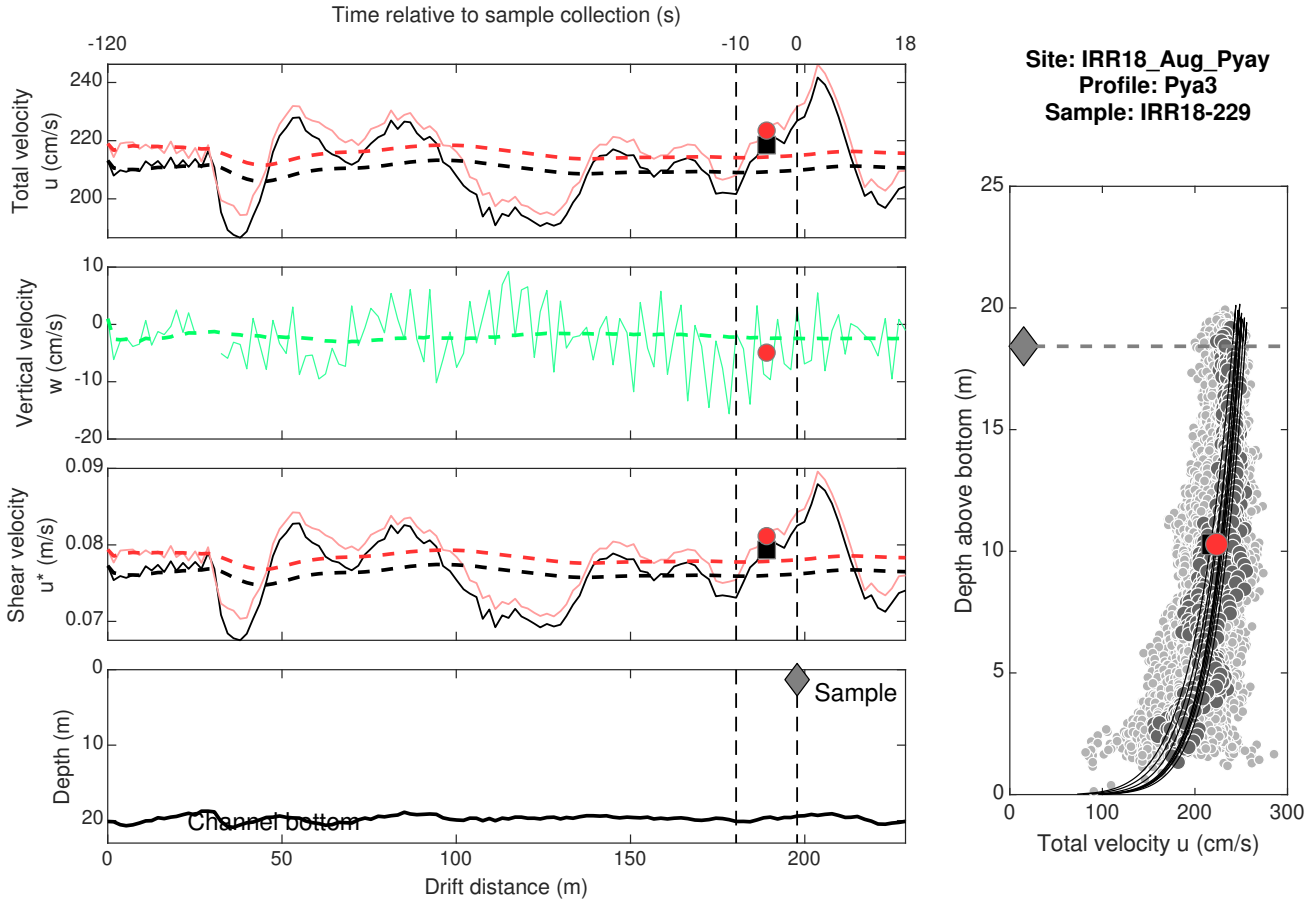

Figure S1. An example of depth-averaged velocity timeseries with relatively stable hydrodynamics, recorded during boat drift before and after suspended sediment sample collection (denoted by the second dashed vertical line). Red circle and lines indicate simple depth-averaged value, whereas black square and lines indicate an integrated power law fit to velocity profile at each timepoint. Thin solids lines are values calculated at each timepoint (approx. 1 s frequency) and thick dashed lines are cumulative time-integrated mean values. The circle and square show the average values calculated for the 10s interval just prior to sample collection (shown by the two dashed vertical lines). Where available, the 10-second power fit integrated mean (black square in panel c) was used in Rouse model fit (Eq. 4) and is given for each sample in Supp. Table S1.

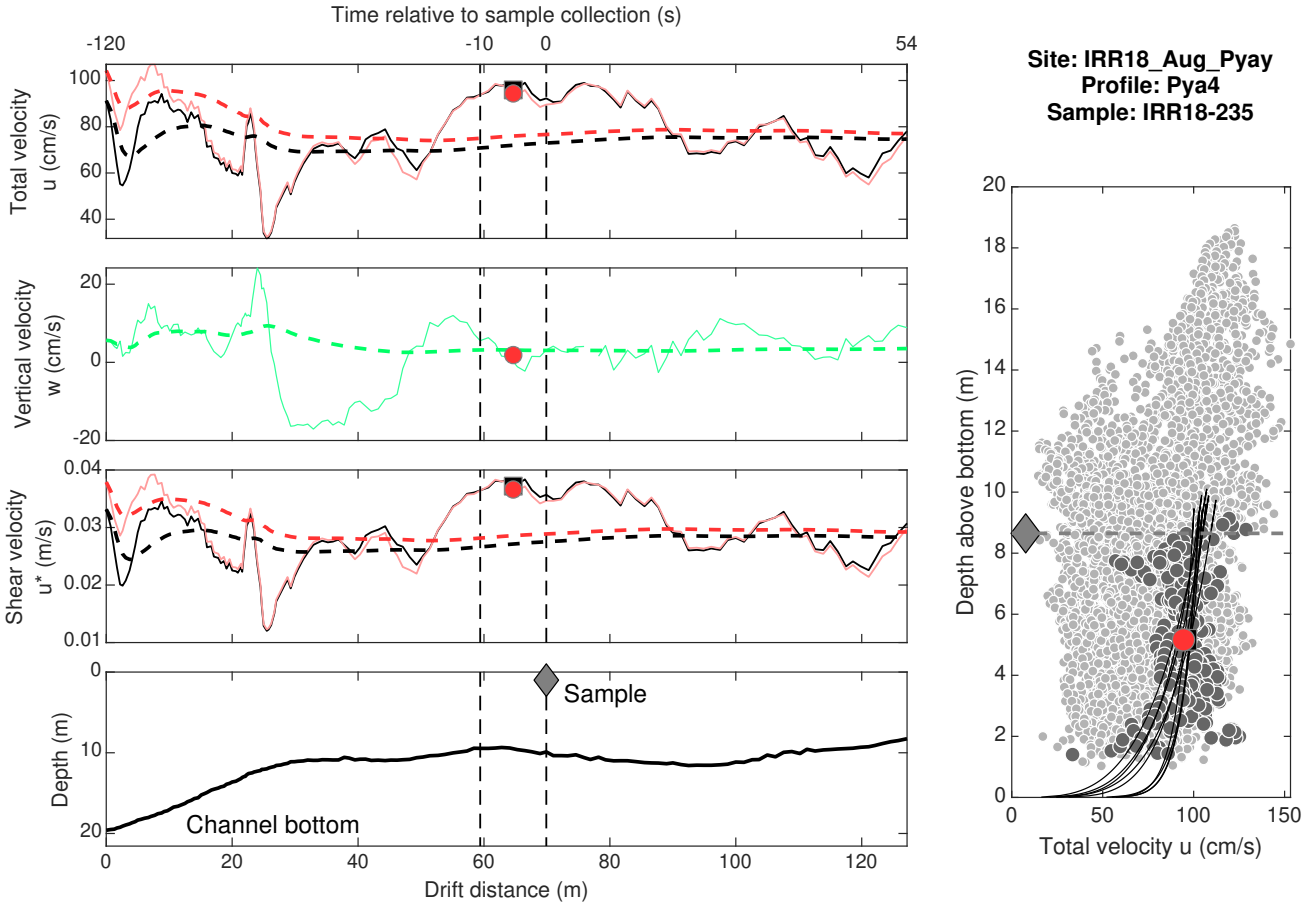

Figure S2. An example of depth-averaged velocity timeseries recorded during boat drift before and after suspended sediment sample collection. Same as symbols as Fig. S1 but showing an example where hydrodynamic conditions change significantly during the drift as the river channel shoals.

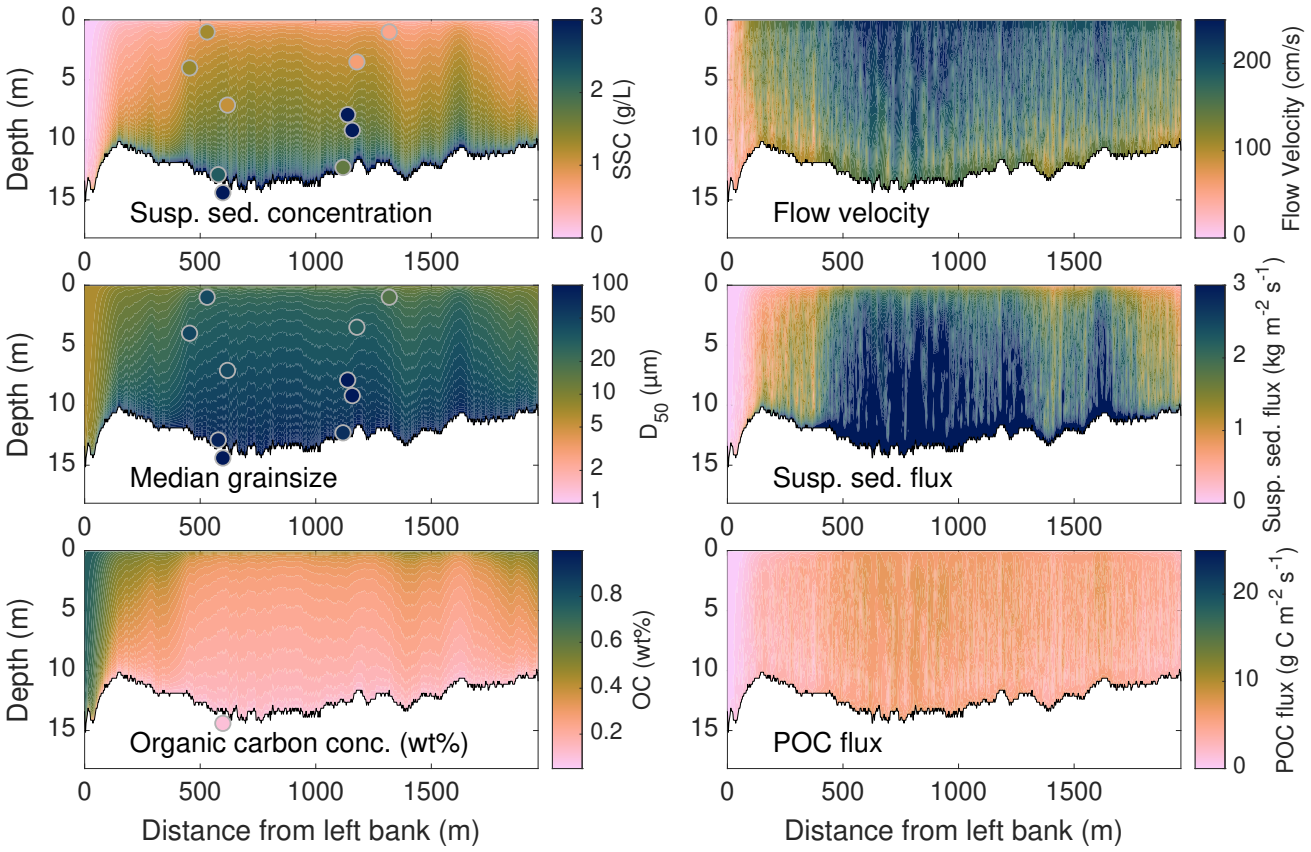

Figure S3. Model results for Irrawaddy (Pyay), August 2017. Colored circles indicate locations and measured compositions of suspended sediment samples.

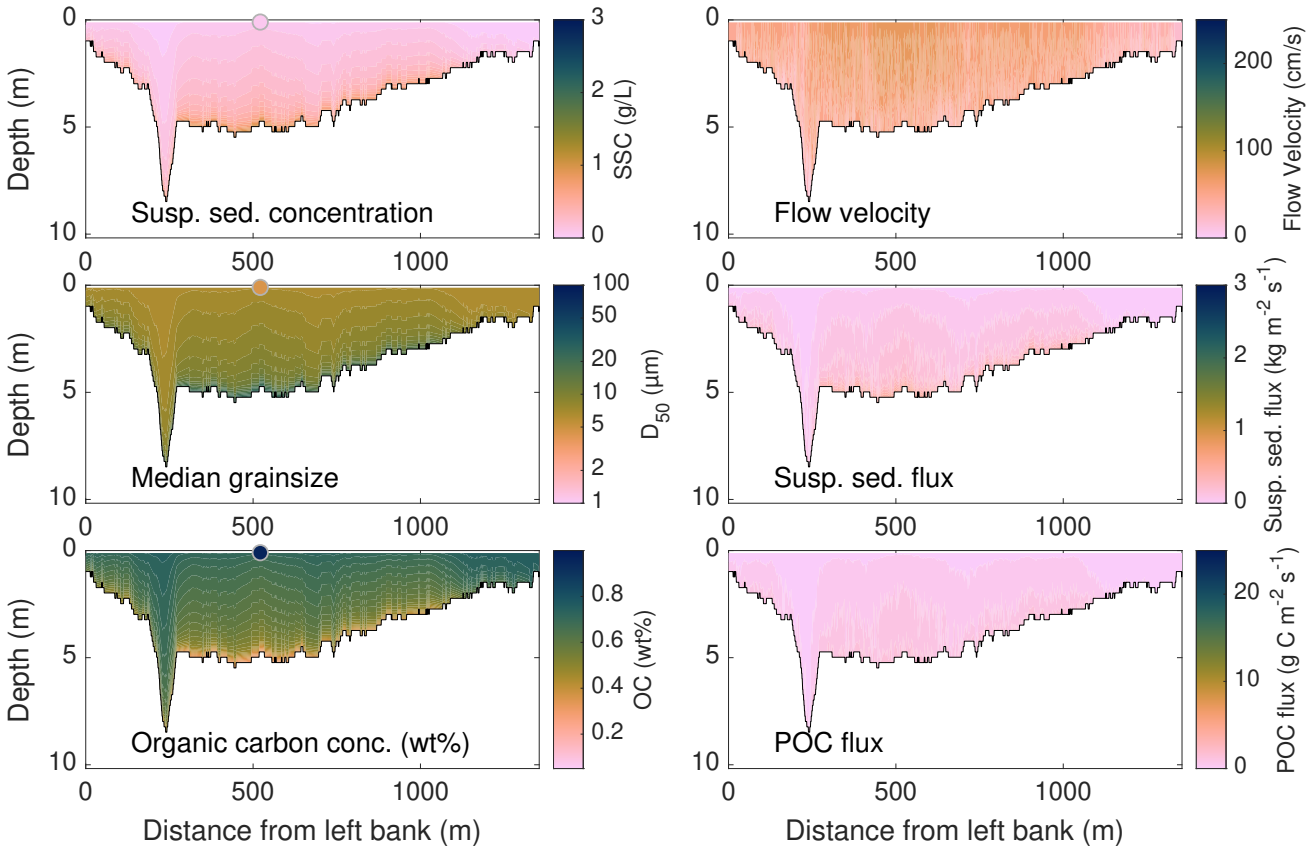

Figure S4. Model results for Irrawaddy (Pyay), February 2018. Colored circles indicate locations and measured compositions of suspended sediment samples.

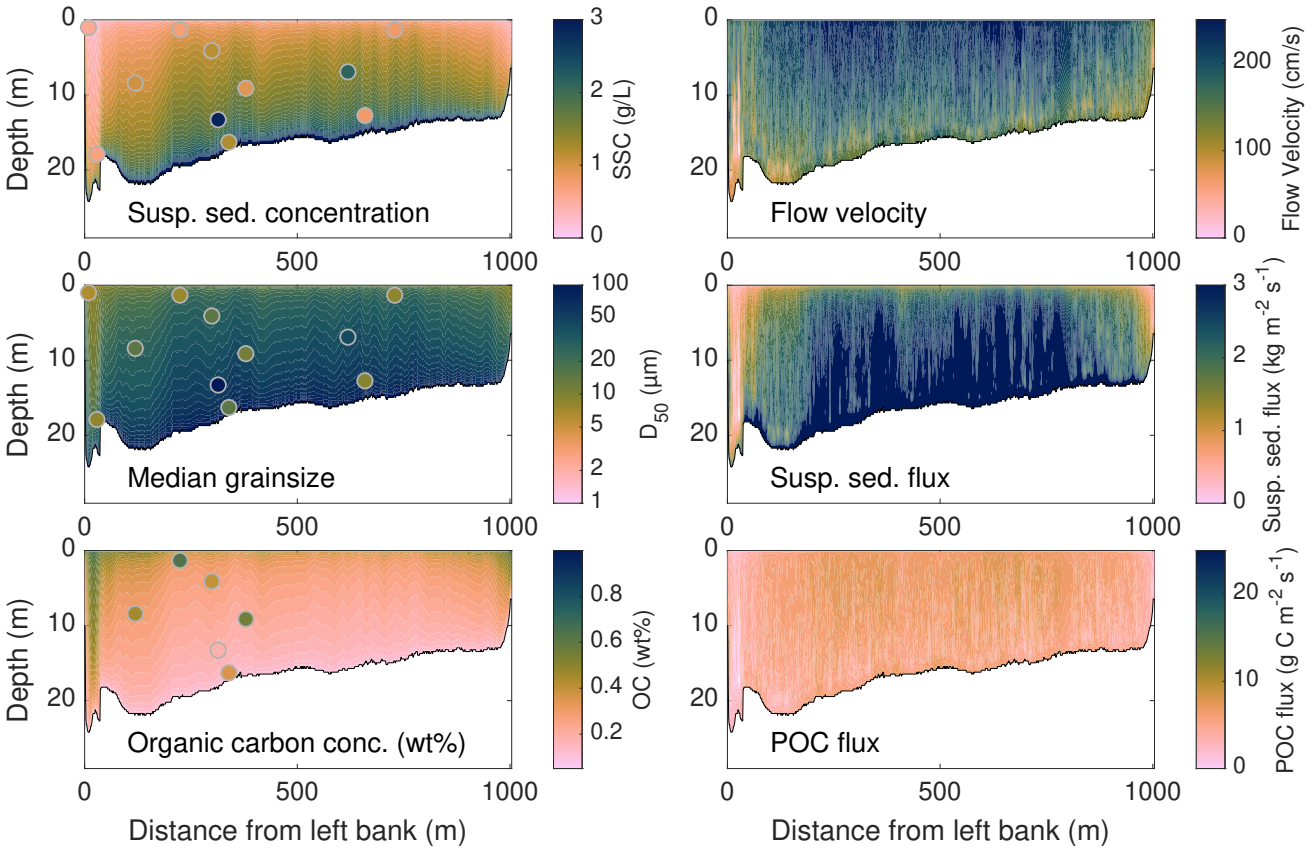

Figure S5. Model results for Irrawaddy (Pyay), August 2018. Colored circles indicate locations and measured compositions of suspended sediment samples.

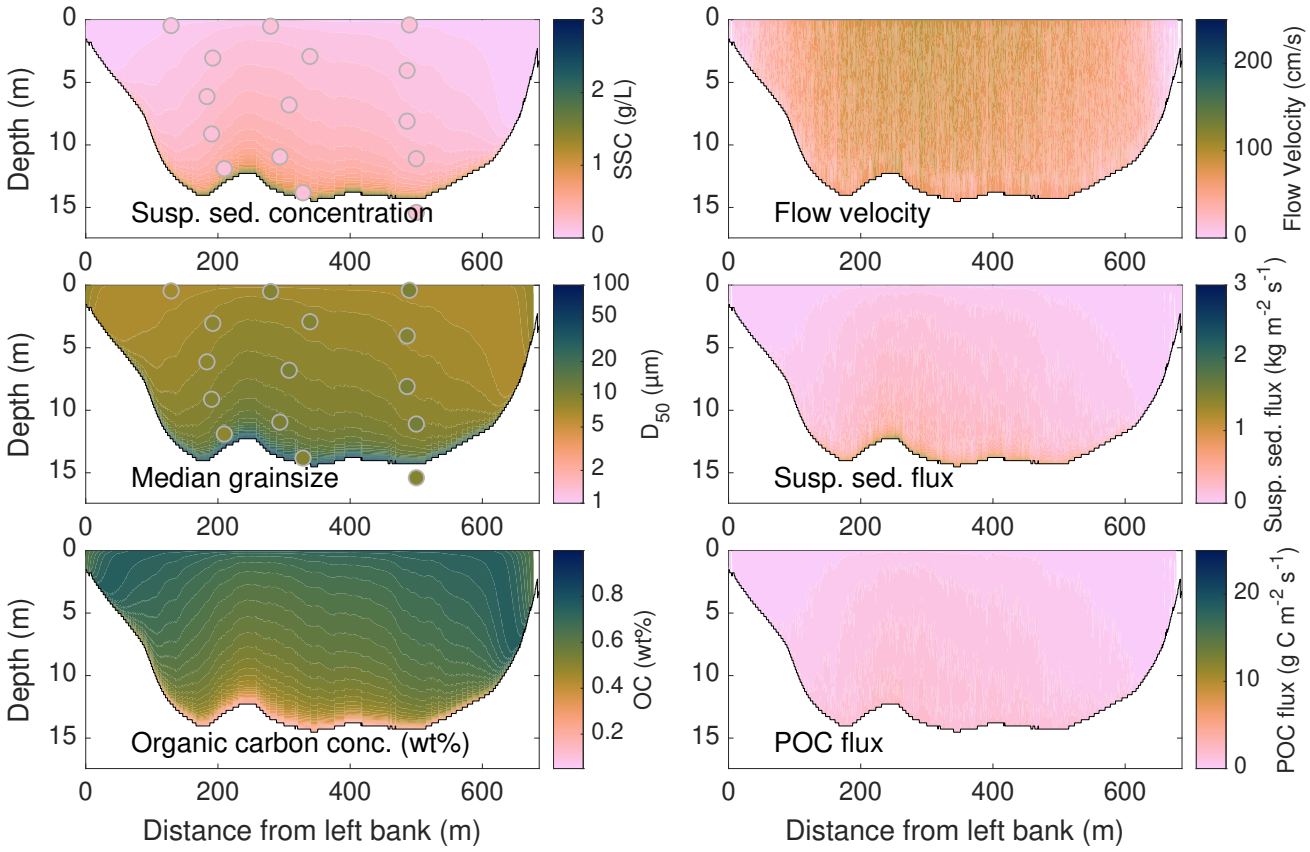

Figure S6. Model results for Irrawaddy (Pyay), May 2019. Colored circles indicate locations and measured compositions of suspended sediment samples.

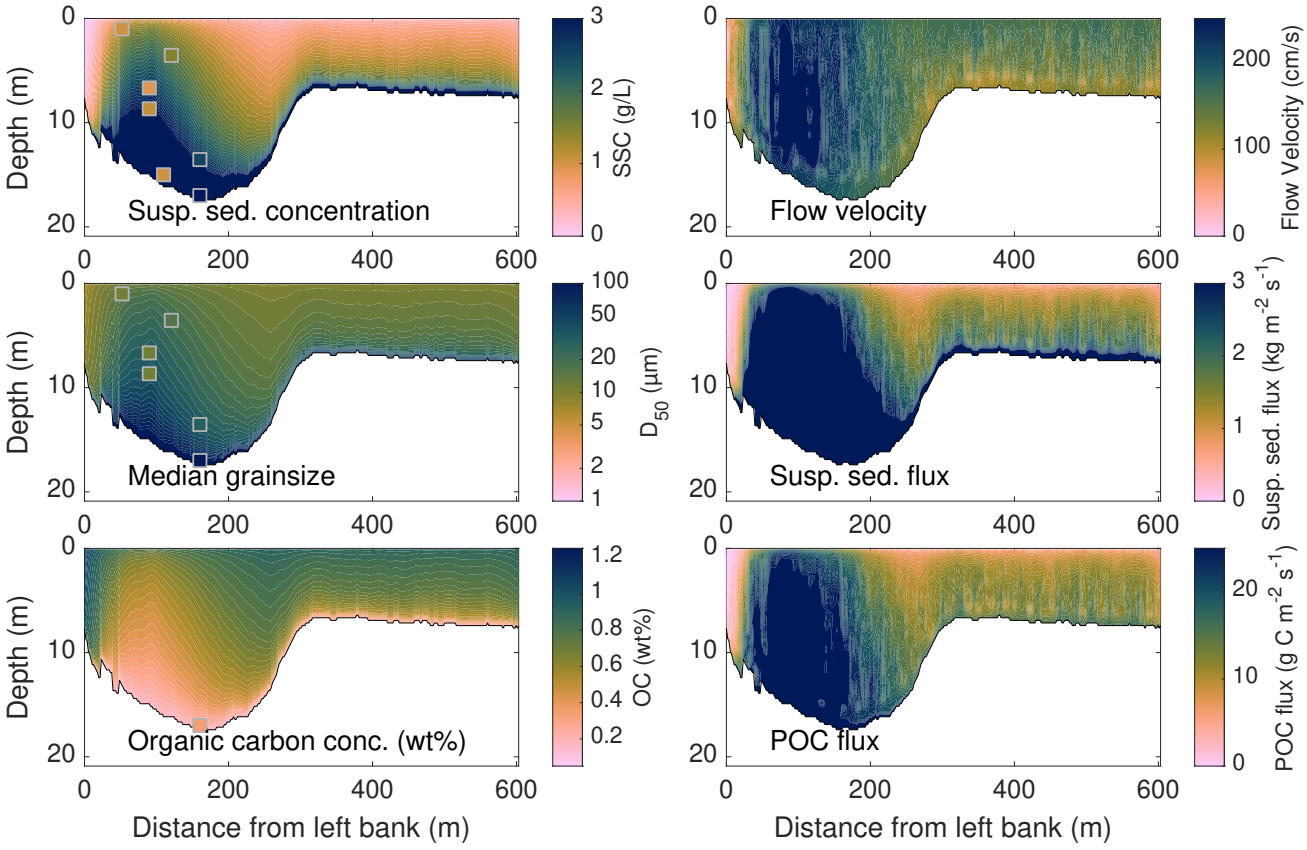

Figure S7. Model results for Salween (Hpa-An), August 2017. Colored squares indicate locations and measured compositions of suspended sediment samples.

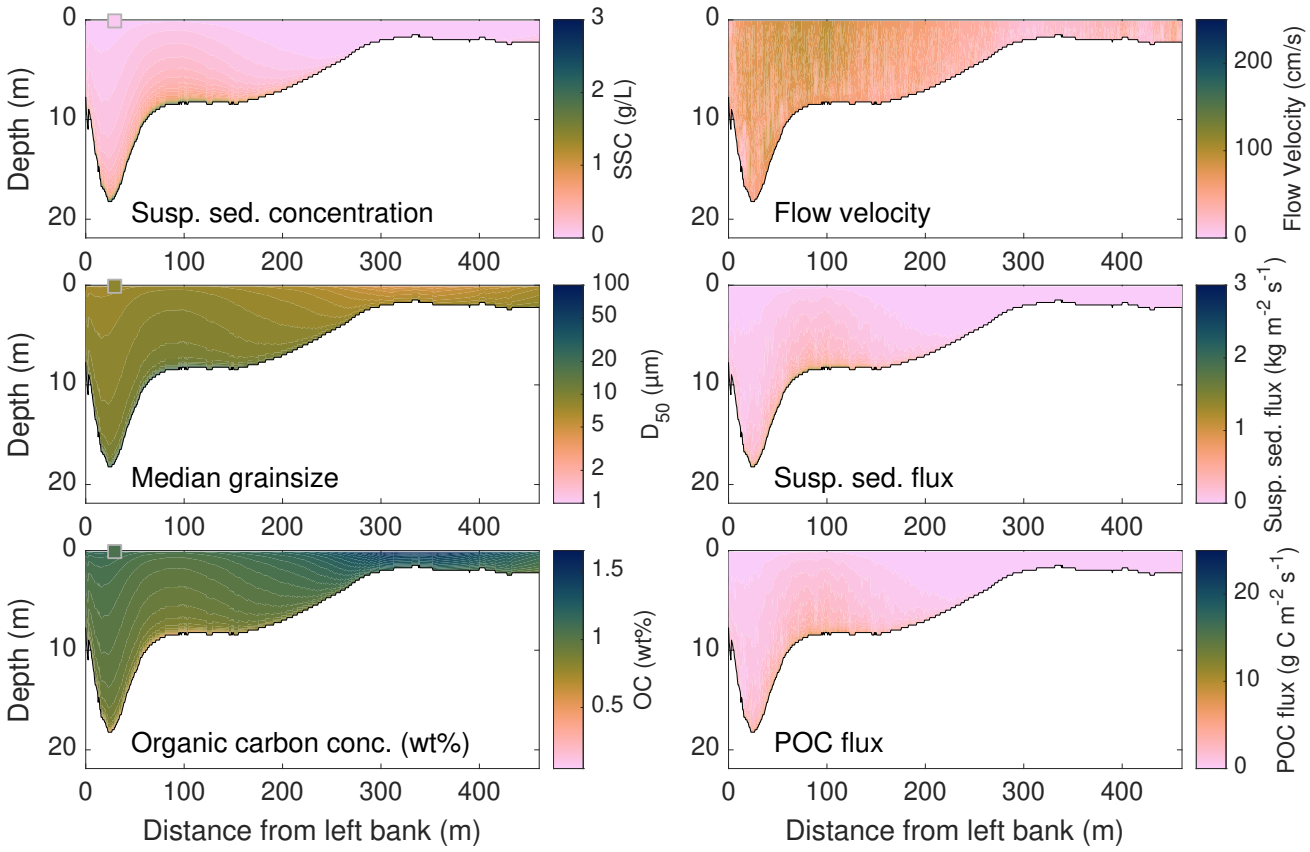

Figure S8. Model results for Salween (Hpa-An), February 2018. Colored squares indicate locations and measured compositions of suspended sediment samples.

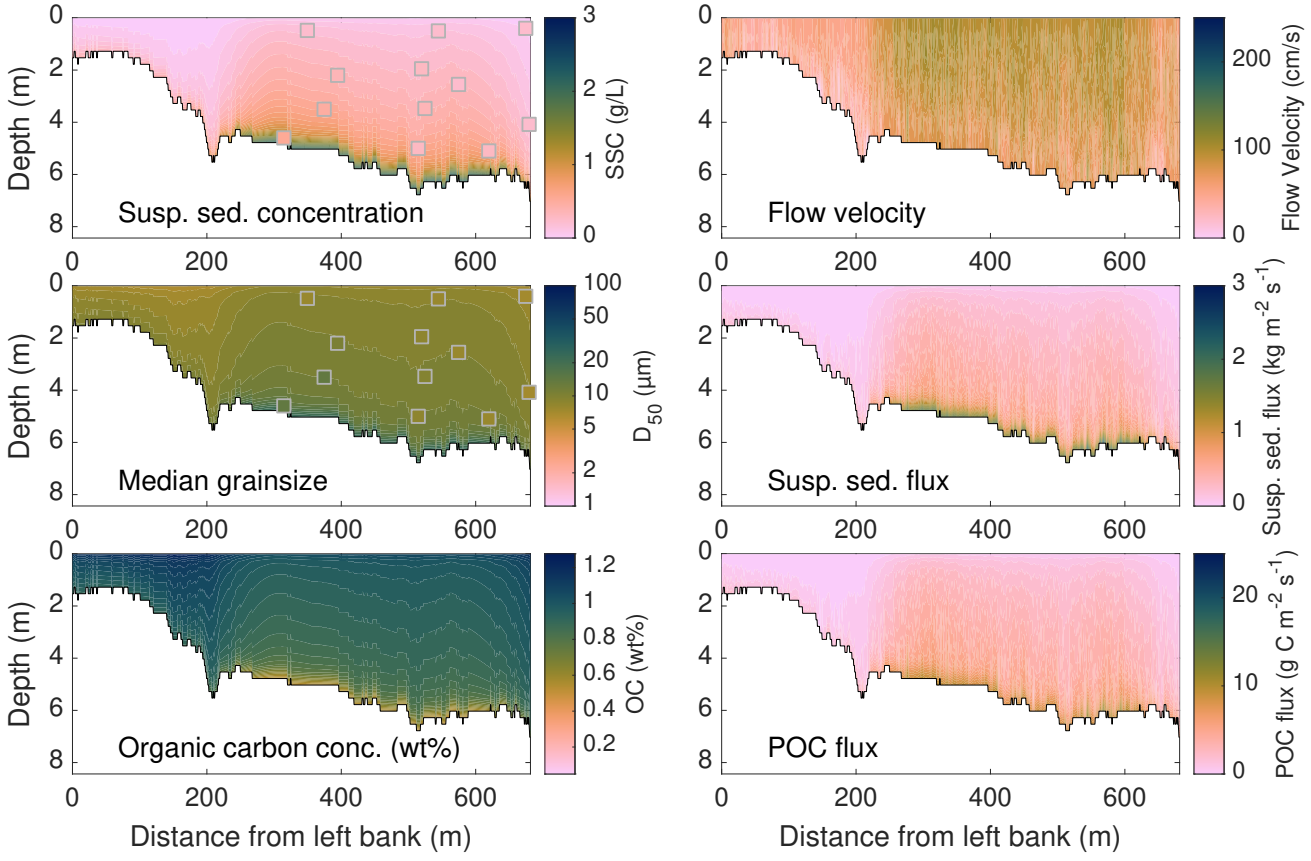

Figure S9. Model results for Salween (Hpa-An), May 2019. Colored squares indicate locations and measured compositions of suspended sediment samples.